

Vasylyev, SS, Filippenko, AV, Vogl, C, Brink, TG, Brown, PJ, Jaeger, TD, Matheson, T, Gal-Yam, A, Mazzali, PA, Modjaz, M, Patra, KC, Rowe, M, Smith, N, Van Dyk, SD, Williamson, M, Yang, Y, Zheng, WK, deGraw, A, Fox, OD, Gates, EL, Jennings, C and Rich, RM

Early-time Ultraviolet Spectroscopy and Optical Follow-up Observations of the Type IIP Supernova 2021yja

<http://researchonline.ljmu.ac.uk/id/eprint/17816/>

Article

Citation (please note it is advisable to refer to the publisher's version if you intend to cite from this work)

Vasylyev, SS, Filippenko, AV, Vogl, C, Brink, TG, Brown, PJ, Jaeger, TD, Matheson, T, Gal-Yam, A, Mazzali, PA, Modjaz, M, Patra, KC, Rowe, M, Smith, N, Van Dyk, SD, Williamson, M, Yang, Y, Zheng, WK, deGraw, A, Fox, OD, Gates, EL, Jennings, C and Rich, RM (2022) Early-time Ultraviolet

LJMU has developed **LJMU Research Online** for users to access the research output of the University more effectively. Copyright © and Moral Rights for the papers on this site are retained by the individual authors and/or other copyright owners. Users may download and/or print one copy of any article(s) in LJMU Research Online to facilitate their private study or for non-commercial research. You may not engage in further distribution of the material or use it for any profit-making activities or any commercial gain.

The version presented here may differ from the published version or from the version of the record. Please see the repository URL above for details on accessing the published version and note that access may require a subscription.

For more information please contact researchonline@ljmu.ac.uk

<http://researchonline.ljmu.ac.uk/>



Early-time Ultraviolet Spectroscopy and Optical Follow-up Observations of the Type IIP Supernova 2021yja

Sergiy S. Vasylyev^{1,2} , Alexei V. Filippenko¹ , Christian Vogl³ , Thomas G. Brink¹ , Peter J. Brown⁴ , Thomas de Jaeger⁵ , Thomas Matheson⁶ , Avishay Gal-Yam⁷ , Paolo A. Mazzali^{3,8} , Maryam Modjaz⁹ , Kishore C. Patra^{1,10} , Micalyn Rowe⁴ , Nathan Smith¹¹ , Schuyler D. Van Dyk¹² , Marc Williamson⁹ , Yi Yang^{1,13}, WeiKang Zheng¹ , Asia deGraw¹, Ori D. Fox¹⁴ , Elinor L. Gates¹⁵ , Connor Jennings¹, and R. Michael Rich¹⁶

¹ Department of Astronomy, University of California, Berkeley, CA 94720-3411, USA; sergiy_vasylyev@berkeley.edu

² Steven Nelson Graduate Fellow

³ Max-Planck-Institut für Astrophysik, Karl-Schwarzschild-Str. 1, D-85748 Garching, Germany

⁴ Mitchell Institute for Fundamental Physics and Astronomy, Department of Physics and Astronomy, Texas A&M University, 4242 TAMU, College Station, TX, USA

⁵ Institute for Astronomy, University of Hawaii, 2680 Woodlawn Drive, Honolulu, HI 96822, USA

⁶ NSF's National Optical-Infrared Astronomy Research Laboratory, 950 North Cherry Avenue, Tucson, AZ 85719, USA

⁷ Department of Particle Physics and Astrophysics, Weizmann Institute of Science, 76100 Rehovot, Israel

⁸ Astrophysics Research Institute, Liverpool John Moores University, 146 Brownlow Hill, Liverpool L3 5RF, UK

⁹ Center for Cosmology and Particle Physics, Department of Physics, New York University, New York, NY 10003, USA

¹⁰ Nagaraj-Noll-Otellini Graduate Fellow

¹¹ Steward Observatory, University of Arizona, 933 North Cherry Avenue, Tucson, AZ 85721, USA

¹² Caltech/IPAC, Mailcode 100-22, Pasadena, CA 91125, USA

¹³ Bengier-Winslow-Robertson Postdoctoral Fellow

¹⁴ Space Telescope Science Institute, 3700 San Martin Drive, Baltimore, MD 21218, USA

¹⁵ UCO/Lick Observatory, P.O. Box 85, Mount Hamilton, CA 95140, USA

¹⁶ Department of Physics and Astronomy, University of California, Los Angeles, CA 90095-1547, USA

Received 2022 March 14; revised 2022 May 6; accepted 2022 May 10; published 2022 August 1

Abstract

We present three epochs of early-time ultraviolet (UV) and optical HST/STIS spectroscopy of the young, nearby Type IIP supernova (SN) 2021yja. We complement the HST data with two earlier epochs of Swift UVOT spectroscopy. The HST and Swift UVOT spectra are consistent with those of other well-studied Type IIP SNe. The UV spectra exhibit rapid cooling at early times, while less dramatic changes are seen in the optical. We also present Lick/KAIT optical photometry up to the late-time tail phase, showing a very long plateau and shallow decline compared with other SNe IIP. Our modeling of the UV spectrum with the TARDIS radiative transfer code produces a good fit for a high-velocity explosion, a low total extinction $E(B - V) = 0.07$ mag, and a subsolar metallicity. We do not find a significant contribution to the UV flux from an additional heating source, such as interaction with the circumstellar medium, consistent with the observed flat plateau. Furthermore, the velocity width of the Mg II $\lambda 2798$ line is comparable to that of the hydrogen Balmer lines, suggesting that the UV emission is confined to a region close to the photosphere.

Unified Astronomy Thesaurus concepts: Type II supernovae (1731); Core-collapse supernovae (304); Ultraviolet astronomy (1736)

Supporting material: data behind figure

1. Introduction

Type II supernovae (SNe II) are defined by the presence of hydrogen in their spectra. They can be photometrically distinguished by their light-curve shape; an SN II with a linearly (in magnitudes) declining light curve is designated as IIL, whereas an SN II displaying an extended plateau lasting ~ 90 days after explosion is classified as IIP. However, the distinction between SNe IIP and IIL is not clear, with recent works suggesting that these subtypes instead constitute a continuum (Anderson et al. 2014a; Valenti et al. 2016). The explosion mechanism producing Type II and a subset of Type I (Ib/Ic; stripped-envelope) SNe is widely accepted to be the core collapse of a star with a zero-age main-sequence mass

$\geq 8 M_{\odot}$; see Filippenko (1997) for a review. The spectral continuum of an SN II peaks in the ultraviolet (UV) in the days and weeks following the explosion and then continues to shift toward optical and near-infrared (NIR) wavelengths over the next few months through a combination of cooling and line blanketing.

It is generally accepted that the progenitors of SNe IIP are red supergiants (RSGs; Smartt et al. 2009; Van Dyk et al. 2011; Smartt 2015; Van Dyk 2017). However, among directly detected progenitors of SNe IIP, progenitors with masses as high as the most massive RSGs seen in nearby stellar populations seem to be missing, in what is known as the “red supergiant problem” (Smartt et al. 2009; Davies & Beasor 2020). Preceding core collapse, an RSG maintains a significant fraction of its hydrogen envelope despite losing some of its initial mass to stellar winds. Upon collapse, the infalling material rebounds off of the newly formed neutron star and is further accelerated by interactions with neutrinos. A shock wave propagates outward, depositing 10%–20% of the



Original content from this work may be used under the terms of the [Creative Commons Attribution 4.0 licence](https://creativecommons.org/licenses/by/4.0/). Any further distribution of this work must maintain attribution to the author(s) and the title of the work, journal citation and DOI.

neutrino energy ($1\text{--}2 \times 10^{52}$ erg) into the expansion of the material and leading to ejecta velocities that reach $\sim 0.1c$. A consequence of this explosion model is that one can approximate the expansion as homologous. Thus, assuming a spherically symmetric explosion, the radius of the photosphere (where optical depth $\tau = 2/3$) is proportional to the photospheric velocity, $r_{\text{ph}} = v_{\text{ph}}t$ (Kirshner & Kwan 1974; Dessart & Hillier 2005a).

Although the optical spectra of core-collapse SNe (CCSNe) have been extensively studied, work on UV radiation has been relatively lacking. Such observations are challenging because rapid follow-up spectroscopy within ~ 1 week after the SN explosion is required from space-based telescopes, before the UV radiation peak has shifted to longer wavelengths. Additionally, SNe need to be sufficiently nearby to enable a decent signal-to-noise ratio (S/N) in the UV. However, several programs have made significant progress in UV spectroscopy of SNe IIP, and we will refer to them throughout this work.

In general, CCSNe exhibit diverse UV/optical spectra. However, SNe IIP have shown some uniformity in their UV spectra. Works by the Swift and Galaxy Evolution Explorer satellites have revealed similarities in the shapes of the UV spectra for SN 1999em-like SNe (Gal-Yam et al. 2008; Bufano et al. 2009; SNe 2005cs, 2005ay, 2006bp). On the other hand, the sample is sparse and mostly comes from a subset of SNe observed by the Hubble Space Telescope (HST) and Swift Ultraviolet/Optical Telescope (UVOT) programs. Although spectroscopically similar in the optical to SNe IIP, SNe IIL (e.g., SNe 1979c and 1980K; Panagia et al. 1980) have been shown to exhibit a UV excess below 1500 Å, blueshifted Mg II line emission, and a smooth continuum suggesting interaction with circumstellar material (CSM; Panagia et al. 1980).

The UV spectra of SNe IIP are not only similar in the shape of the continuum but also in spectral features. This includes the prominent Mg II $\lambda 2798$ P Cygni profile, as well as emission “bumps” around 2200, 2400, and 2600 Å. These emission features are associated with blended Fe II and Ni II lines (Brown et al. 2007; Gal-Yam et al. 2008; Bufano et al. 2009; Dhungana et al. 2016).

Early-time UV spectra convey important information about the kinematics of the fast-expanding ejecta, the temporal evolution of the photospheric temperature, and the metal content of the progenitor star (Mazzali 2000; Dessart & Hillier 2005b, 2006). The line-of-sight extinction may also be well determined through spectroscopic modeling of the UV. Moreover, the UV flux is an excellent probe of the circumstellar environment in the vicinity of the SN, allowing one to identify additional heating sources such as CSM interaction (Ben-Ami et al. 2015). In this work, we present five early-time UV spectra along with optical spectra and photometry of a relatively nearby SN IIP.

On 2021 September 8, SN 2021yja (AT 2021yja) was discovered at 13:12:00 (UTC dates are used throughout this paper) in the spiral galaxy NGC 1325 by the Asteroid Terrestrial-impact Last Alert System (ATLAS; Tonry et al. 2018); see AstroNote 2021–235 (Smith et al. 2021). A redshift of $z = 0.005307$ was reported by Springob et al. (2005), and a median distance of 21.8 Mpc can be queried from the NASA/IPAC Extragalactic Database (NED). Imaging obtained with the MuSCAT3 instrument on the Faulkes-North Telescope (FTN) at Haleakala, Hawai‘i, reported a transient consistent with SN 2021yja on 2021 September 7 at 15:02:28 (AstroNote

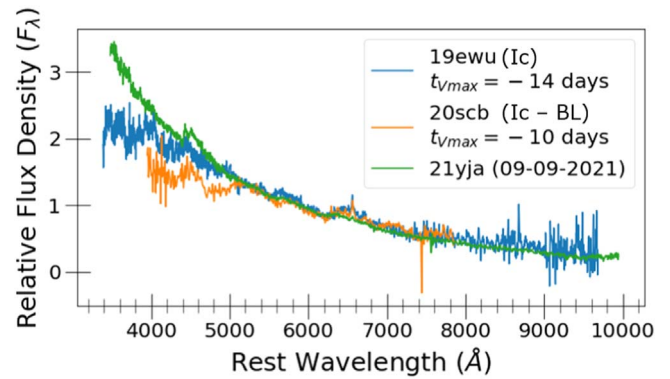


Figure 1. Very early time spectroscopy of SN 2021yja (green) compared to Type Ic/Ic-BL SNe 2019ewu (blue; Hiramatsu et al. 2019; Williamson et al. in preparation) and 2020scb (orange; Smith et al. 2020).

2021–236; Kilpatrick 2021). We adopt the midpoint between the last nondetection (2021 September 6 at 11:32:38) and the first detection (2021 September 8 at 13:12:00) as an estimated time of explosion, 2021 September 7.5. All phases will be given in days relative to this date throughout the paper.

In Figure 1, we compare our earliest optical spectrum of SN 2021yja obtained on 2021 September 9.5 (+2 days) by the FLOYDS spectrograph mounted on the FTN (Pellegrino et al.) with early-time spectra of Type Ic SN 2019ewu (Hiramatsu et al. 2019; Williamson et al. 2022, in preparation) and Type Ic-BL SN 2020scb (Smith et al. 2020) at similar phases; there is a close resemblance. Although weak, broad H α emission might be present in the spectrum of SN 2021yja, this feature is even more prominent in the spectra of SNe 2019ewu (Ic) and SN 2020scb (Ic-BL).

Moreover, all three objects exhibit a small bump near 4600 Å superposed on a blue, otherwise relatively featureless continuum. Hence, we triggered SN 2021yja for our Cycle 28 HST program that targeted stripped-envelope SNe (GO-16178; PI: A. V. Filippenko).

Later, it became clear that the optical spectrum of SN 2021yja was transforming into that of an SN II, and the optical photometry was consistent with the Type IIP subtype, but the HST observations had already begun, and the object was deemed sufficiently interesting to continue monitoring. The spectra presented in this paper make SN 2021yja one of the few SNe IIP studied with early (9 days after explosion), high-S/N (~ 35) UV data.

The paper is organized as follows. Section 2 presents further discussion of this topic and a summary of our observations. In Section 3, we discuss the spectroscopic analysis of SN 2021yja using a Monte Carlo radiative transfer code, TARDIS. We conclude in Section 4.

2. Observations and Data Analysis

2.1. HST/STIS

The SN 2021yja was observed as an HST disruptive target of opportunity on 2021 September 16 (+9 days after explosion), 2021 September 21 (+14 days), and 2021 September 28 (+21 days) using the CCD ($52'' \times 52''$ field of view) detector of the Space Telescope Imaging Spectrograph (STIS). Although the onboard Near-UV Multi-Anode MicroChannel Array detectors do not suffer from read noise and charge transfer efficiency like the CCDs, they do have bright-object limits

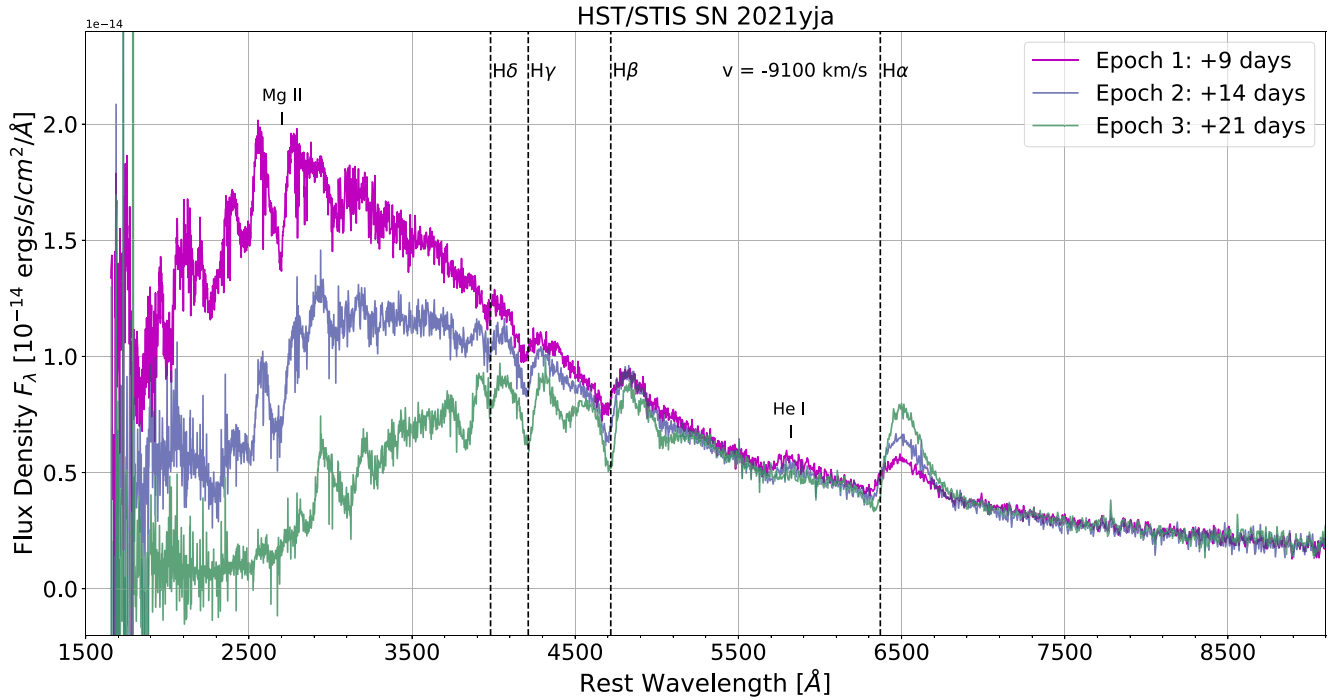


Figure 2. The HST/STIS UV-optical spectra of SN 2021jya. No normalization has been applied; in other words, there is a general agreement in the flux density at optical wavelengths, while the UV varies dramatically. The wavelength scale has been corrected to the rest frame using the recession velocity of the host galaxy. Balmer lines at an expansion velocity of $v = -9100 \text{ km s}^{-1}$ are marked by vertical dotted lines.

Table 1
HST Observation Log for SN 2021jya

Date (UTC)	Exp. (s)	Grating/Filter	$\Delta\lambda$ (Å)
2021-09-16	2060	G230LB	1685–3060
2021-09-16	2340	G230LB	1685–3060
2021-09-16	2340	G230LB	1685–3060
2021-09-16	2000	G230LB	1685–3060
2021-09-16	2340	G230LB	1685–3060
2021-09-16	1544	G230LB	1685–3060
2021-09-16	200	G430L	2900–5700
2021-09-16	100	G750L	5240–10270
<hr/>			
2021-09-21	2060	G230LB	1685–3060
2021-09-21	2340	G230LB	1685–3060
2021-09-21	2340	G230LB	1685–3060
2021-09-21	2000	G230LB	1685–3060
2021-09-21	1544	G230LB	1685–3060
2021-09-21	200	G430L	2900–5700
2021-09-21	100	G750L	5240–10270
<hr/>			
2021-09-28	2060	G230LB	1685–3060
2021-09-28	2340	G230LB	1685–3060
2021-09-28	2340	G230LB	1685–3060
2021-09-28	2000	G230LB	1685–3060
2021-09-28	2340	G230LB	1685–3060
2021-09-28	1544	G230LB	1685–3060
2021-09-28	200	G430L	2900–5700
2021-09-28	100	G750L	5240–10270

Table 2
Kast Spectroscopy of SN 2021jya^a

UT Date (YYYY-MM-DD)	Phase ^b (days)	Average Airmass	Seeing (arcsec)	Red Chan. Total Exposure (s) ^c
2021-09-11	4	1.9	3	900
2021-09-12	5	1.9	1.7	900
2021-09-13	6	2.0	2	600 ^d
2021-10-07	30	2.0	2	500
2021-10-15	38	2.0	2	1200
2021-11-03	57	2.4	1.2	1200
2021-11-07	61	3.0	2.6	1200
2021-11-12	66	2.2	1.2	1200
2021-12-11	95	2.0	1.3	1200
2022-01-06	121		1.2	1500

Notes.

^a The wavelength range was 3632–10754 Å for each observation.

^b Days after explosion assuming 2021 September 7 as the explosion date.

^c The blue channel exposure time was 60 s longer on each date.

^d Only one exposure was taken with the red channel.

For epochs 1 and 3, observations of the mid-UV (MUV; 1685–3060 Å) with the G230LB grating were made over six visits, whereas epoch 2 had only five visits. Only one visit per epoch was made for the near-UV (NUV; 2900–5700 Å) and optical (5240–10270 Å) with the G430L and G750L gratings, respectively. A detailed observation log can be found in Table 1, and the three HST spectra are shown in Figure 2.

(Prichard et al. 2022). We used the CCD mode to avoid saturating the detector (although, in retrospect, the UV flux had fallen sufficiently by the epoch of the first HST observation), and also because there were fewer scheduling constraints (we did not have to avoid the South Atlantic Anomaly).

2.2. Lick Observatory Kast Spectra and KAIT Photometry

Optical spectra of SN 2021jya were obtained using the Kast Double Spectrograph on the Shane 3 m telescope at Lick

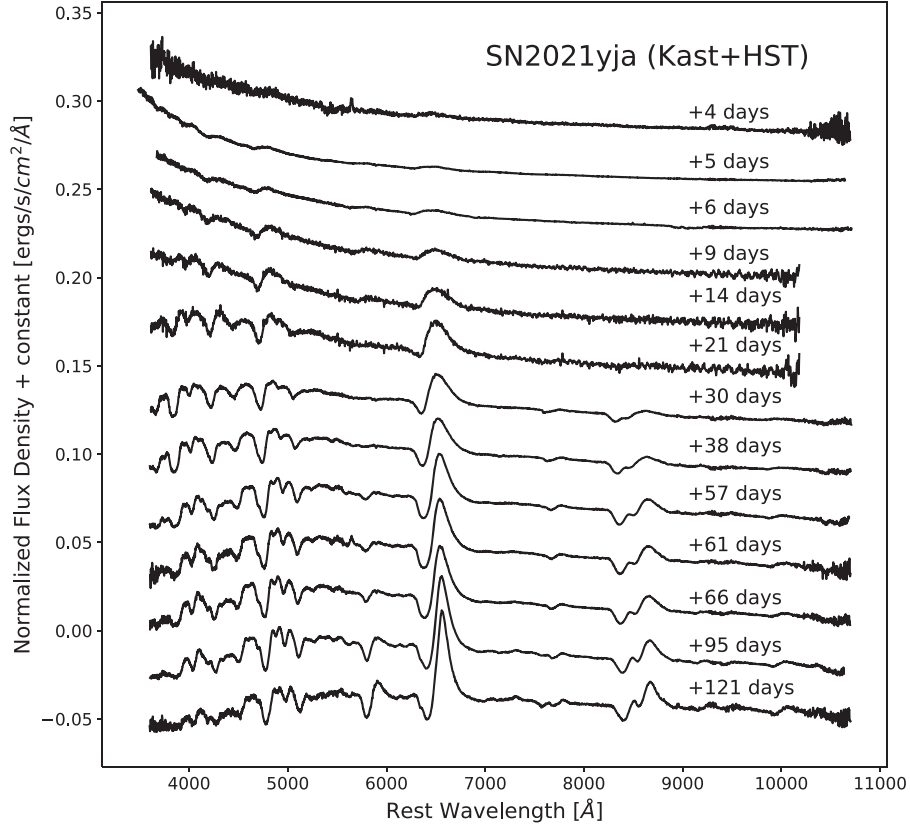


Figure 3. Optical spectral time series of SN 2021yja observed with Kast and HST/STIS (days +9, +14, and +21). The wavelength scale has been corrected to the rest frame using the recession velocity of the host galaxy.

(The data used to create this figure are available.)

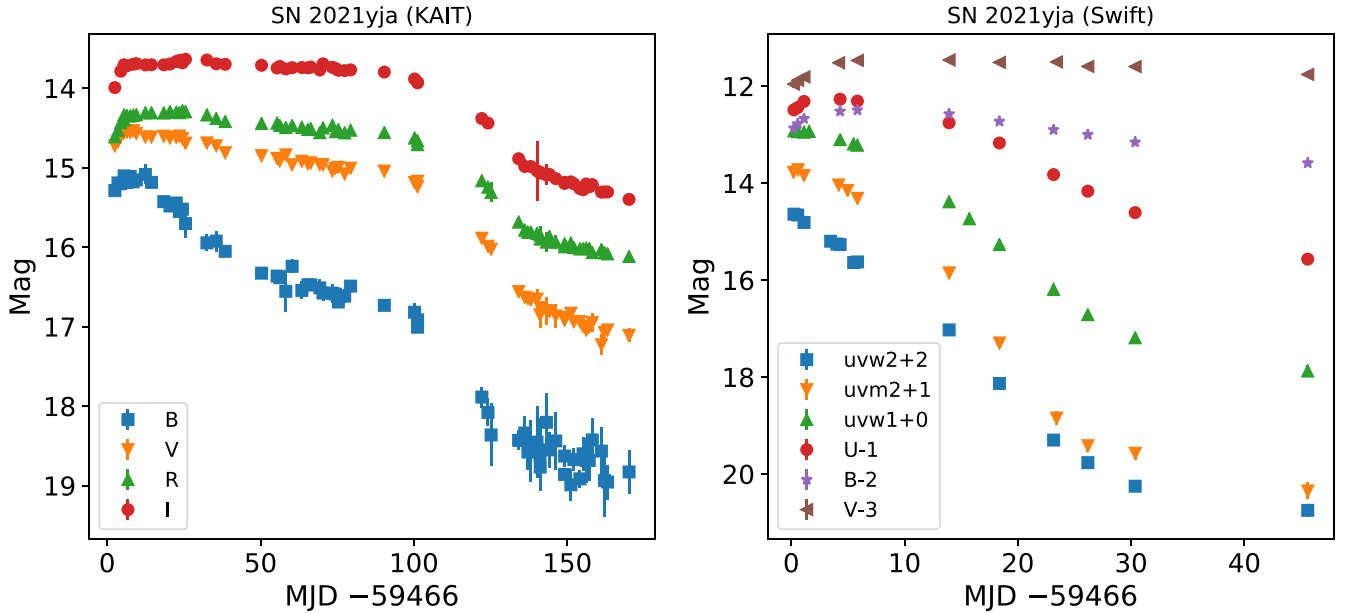


Figure 4. KAIT and Swift photometry of SN 2021yja in apparent magnitudes. No extinction corrections have been applied to the data.

Observatory (Miller et al. 1988; Miller & Stone 1993). The spectral sequence consists of 10 epochs and spans +4 to +121 days. All observations cover a wavelength range from 3632 to 10754 Å. Observations and data reduction were carried out following the techniques described by Silverman et al.

(2012) and Shivvers et al. (2013). The Kast observation log is shown in Table 2. To facilitate cosmic-ray removal, observations consisted of three exposures in the red channel (which employs a thick CCD), each one-third of the exposure time in Table 2 (but note that only a single red channel exposure was

Table 3
KAIT/Nickel Photometry of SN 2021yja

Date (MJD)	<i>B</i> (mag)	<i>V</i> (mag)	<i>R</i> (mag)	Clear (mag)	<i>I</i> (mag)
59,468.51	14.79(03)	14.72(01)	14.61(01)	14.47(01)	14.49(01)
59,469.54	14.69(04)	14.67(02)	14.53(02)	14.41(05)	...
59,470.44	14.70(02)	14.60(01)	14.43(01)	14.39(02)	14.29(01)
59,471.49	14.69(02)	14.56(01)	14.40(01)	...	14.22(02)
59,471.54 ^a	14.60(02)	14.48(01)	14.34(01)	...	14.21(01)
59,472.46	14.69(06)	14.55(01)	14.35(01)	14.29(02)	14.22(01)
59,473.53	14.64(04)	14.55(01)	14.35(01)	14.32(03)	...
59,474.50	14.68(03)	14.55(02)	14.34(01)	14.25(01)	14.20(01)
59,475.53	14.65(03)	14.57(01)	14.34(01)	14.28(02)	14.19(02)
59,478.47	14.59(12)	14.61(03)	14.31(02)	14.30(02)	14.21(02)
59,480.45	14.69(05)	14.61(02)	14.31(01)	14.27(03)	14.21(02)
59,484.47	14.93(03)	14.60(02)	14.31(01)	14.31(02)	14.21(02)
59,486.48	14.98(04)	14.62(01)	14.30(01)	14.29(01)	14.20(02)
59,488.55	14.95(05)	14.62(02)	14.31(01)	14.34(01)	14.16(02)
59,489.54	15.05(05)	14.60(02)	14.31(01)	14.32(01)	14.15(02)
59,490.54	15.02(04)	14.63(02)	14.29(01)	14.34(01)	14.18(02)
59,491.55	15.20(18)	14.69(06)	14.14(03)
59,498.54	15.45(10)	14.69(03)	14.34(03)	14.41(02)	14.15(04)
59,501.55	15.42(13)	14.72(03)	14.38(03)	14.46(21)	14.19(03)
59,504.49	15.55(04)	14.81(02)	14.42(01)	14.45(01)	14.20(02)
59,516.34	15.83(03)	14.85(01)	14.45(01)	14.49(01)	14.21(02)
59,521.41	15.86(04)	14.88(02)	14.44(02)	...	14.25(02)
59,522.29	15.88(04)	14.91(02)	14.47(01)	14.52(01)	14.23(02)
59,524.24	16.06(26)	14.84(05)	14.50(03)	14.52(02)	14.26(03)
59,526.32	15.74(09)	14.96(03)	14.47(02)	...	14.24(02)
59,529.48	16.04(11)	14.92(04)	14.49(02)	14.59(02)	14.24(03)
59,531.45	15.97(04)	14.95(02)	14.52(01)	14.56(01)	14.24(01)
59,532.39	15.97(05)	14.94(02)	14.51(01)	14.60(03)	14.23(02)
59,535.34	16.01(11)	14.96(04)	14.56(03)	14.60(03)	14.27(04)
59,536.37	16.08(09)	14.96(03)	14.50(02)	14.63(03)	14.19(03)
59,539.41	16.08(12)	15.04(04)	14.47(04)	14.57(05)	14.24(05)
59,540.41	16.09(09)	15.01(03)	14.55(02)	14.57(02)	14.25(03)
59,541.37	16.19(05)	15.00(02)	14.52(02)	14.59(01)	14.28(02)
59,543.44	16.12(08)	15.08(03)	14.56(02)	14.60(02)	14.28(02)
59,545.36	15.99(07)	15.01(02)	14.53(02)	14.58(01)	14.27(02)
59,556.36	16.23(05)	15.04(02)	14.56(02)	14.65(02)	14.30(02)
59,566.22	16.32(11)	15.19(05)	14.63(06)	14.73(05)	14.38(05)
59,567.20	16.41(09)	15.24(02)	14.66(02)	14.77(01)	14.43(02)
59,588.14	17.39(13)	15.89(04)	15.17(02)	15.30(01)	14.88(02)
59,590.15	17.58(18)	15.99(04)	15.25(03)	15.40(03)	14.94(03)
59,600.15	17.93(12)	16.56(03)	15.69(02)	15.87(14)	15.39(03)
59,602.14	17.84(21)	16.63(05)	15.79(05)	15.90(02)	15.48(09)
59,603.17	18.08(21)	16.65(05)	15.81(03)	15.92(13)	...
59,604.12	18.07(39)	16.66(05)	15.81(02)	15.94(01)	15.49(03)
59,606.14	17.95(45)	16.65(13)	15.83(04)	16.02(03)	15.54(37)
59,607.11	18.11(46)	16.85(16)	15.85(12)	16.01(02)	15.56(04)
59,607.19 ^a	18.27(04)	16.76(02)	15.90(02)	...	15.57(02)
59,609.21	17.70(36)	16.80(18)	15.94(13)	16.04(02)	15.59(13)
59,610.19	18.05(22)	16.80(08)	15.87(03)	16.04(02)	15.58(03)
59,612.23	17.94(36)	16.87(15)	15.94(08)	16.05(08)	15.64(07)
59,615.11 ^a	18.36(05)	16.88(02)	16.00(02)	...	15.68(02)
59,615.14	18.13(14)	16.92(04)	15.96(02)	16.11(05)	15.70(04)
59,617.17	18.49(20)	16.83(05)	15.95(03)	16.13(02)	15.68(03)
59,618.15	18.17(14)	16.94(04)	16.01(03)	16.15(04)	15.70(03)
59,620.11 ^a	18.41(11)	16.93(03)	16.02(03)	...	15.76(03)
59,621.16	18.10(21)	17.00(07)	16.02(04)	16.20(07)	15.78(06)
59,622.17	18.19(28)	17.04(06)	16.02(03)	16.19(08)	15.71(05)
59,623.17	18.18(25)	17.00(06)	16.02(03)	16.19(08)	15.74(04)
59,624.17	17.93(27)	16.95(12)	16.07(06)	16.18(09)	15.72(09)
59,627.13	18.07(30)	17.23(13)	16.03(05)	16.27(04)	15.81(05)
59,628.14	18.44(45)	17.07(08)	16.07(03)	16.27(03)	15.81(04)
59,629.14	18.44(22)	17.04(06)	16.09(03)	16.26(02)	15.81(03)

Notes.

^a Observed with Nickel.

obtained on 2021 September 13). The blue channel (thin CCD) was exposed throughout the red channel observations, with an additional 60 s to synchronize readout times. The phase is

rounded to the nearest day relative to explosion. The optical spectra are shown in Figure 3.

Follow-up photometry of SN 2021yja was performed with images from the 0.76 m Katzman Automatic Imaging Telescope (KAIT) as part of the Lick Observatory Supernova Search (Filippenko et al. 2001), as well as with images from the 1 m Nickel telescope at Lick Observatory. The *B*, *V*, *R*, and *I* multiband images were obtained with both telescopes, and additional Clear-band images (similar to *R*; Li et al. 2011) were obtained with KAIT. The KAIT observation log is shown in Table 3.

All images were reduced using a custom pipeline¹⁷ detailed by Stahl et al. (2019). Point-spread function photometry was obtained using DAOPHOT (Stetson 1987) from the IDL Astronomy User's Library.¹⁸ Several nearby stars were chosen from the Pan-STARRS1¹⁹ catalog for calibration. Their magnitudes were first transformed into Landolt magnitudes (Landolt 1992) using the empirical prescription presented by Tonry et al. (2012; see their Equation (6)) and then transformed to the KAIT/Nickel natural system. Apparent magnitudes were all measured in the KAIT4/Nickel2 natural system. The final results were transformed to the standard system using local calibrators and color terms for KAIT4 and Nickel2 (Stahl et al. 2019). The optical light curves are presented in the left panel of Figure 4.

2.3. Swift UVOT

The SN 2021yja was observed photometrically and spectroscopically in the UV with the Neil Gehrels Swift Observatory (Gehrels et al. 2004). The UVOT (Romney et al. 2005) is a Ritchey–Chrétien reflector with a CCD detector. Its wavelength range covers 1600–6000 Å with imaging capabilities in six bandpasses (*uvw2*, *uvm2*, *uvw1*, *u*, *b*, and *v*). Swift observations began on 2021 September 9 at 04:42:34. The UVOT photometry was reduced using the pipeline of the Swift Optical Ultraviolet Supernova Archive (Brown et al. 2014) with the updated sensitivity corrections and an aperture correction calculated using observations from 2021. An observing log of Swift observations is presented in Table 4. The Swift photometry is presented in Figure 4 and Hosseinzadeh et al. (2022).

Swift/UVOT spectroscopy began on 2021 September 12 1:10:19. Data were reduced using the *uvotpy* package (Kuin 2014) and the calibration of Kuin et al. (2015). Table 5 summarizes the Swift/UVOT spectroscopy of SN 2021yja. Spectra collected within ~20 hr were median combined to increase the S/N to ~3 for wavelengths 1800–3600 Å. A total of two spectra (at +5 and +7 days) were obtained and used in further analysis (see Figure 5).

3. Photometric and Spectroscopic Analysis

We ran the Supernova Identification (SNID; Blondin & Tonry 2007) program on our observed Kast spectra of SN 2021yja. Cross-correlation with a library of SN spectra shows that the spectra of SN 2021yja obtained after +6 days exhibit the best matches with the Type IIP SN templates at similar phases (e.g., see Figure 6). The matching of SN 2021yja at even earlier phases failed to converge, since the spectra are almost featureless in the optical. Throughout the rest of the

¹⁷ <https://github.com/benstahl92/LOSSPhotPipeline>

¹⁸ <http://idlastro.gsfc.nasa.gov/>

¹⁹ <http://archive.stsci.edu/panstarrs/search.php>

Table 4
Swift UVOT Photometry of SN 2021yja

Date (MJD)	<i>uvw</i> 2 (mag)	<i>uvm</i> 2 (mag)	<i>uvw</i> 1 (mag)	<i>U</i> (mag)	<i>B</i> (mag)	<i>V</i> (mag)
59,466.2	12.64(04)	12.78(04)	12.93(04)	13.49(04)	14.87(05)	14.96(06)
59,466.6	12.66(04)	12.72(05)	12.94(04)	13.44(04)	14.78(05)	14.88(06)
59,467.1	12.81(04)	12.84(04)	12.95(04)	13.32(04)	14.67(04)	14.81(06)
59,467.6	12.94(04)
59,469.5	13.20(04)
59,470.0	13.26(04)
59,470.2	...	13.04(04)	14.52(06)
59,470.3	13.27(04)	...	13.10(04)	13.27(04)	14.52(04)	...
59,471.0	...	13.15(05)
59,471.5	13.64(04)	...	13.19(04)
59,471.8	13.63(04)	13.32(05)	13.22(04)	13.31(04)	14.50(04)	14.47(06)
59,479.9	15.03(06)	14.85(06)	14.39(06)	13.76(04)	14.57(04)	14.46(06)
59,484.4	16.13(07)	16.30(07)	15.27(06)	14.17(05)	14.73(04)	14.51(06)
59,489.2	17.30(08)	...	16.19(06)	14.82(05)	14.90(05)	...
59,489.4	...	17.85(14)	14.50(06)
59,492.2	17.77(09)	18.42(12)	16.71(08)	15.17(06)	15.00(05)	14.59(06)
59,496.4	18.25(11)	18.57(12)	17.19(09)	15.61(07)	15.16(05)	14.60(06)
59,511.6	18.75(13)	19.35(17)	17.88(12)	16.57(08)	15.58(05)	14.76(05)

Note. Swift/UVOT photometry of 2021yja as presented by Hosseinzadeh et al. (2022). Apparent magnitudes are reported with their 1σ uncertainties as indicated by the number in parentheses and in units of 0.01.

Table 5
Swift UVOT Spectroscopic Observations

Start Time (yyyy-mm-dd hh:mm:ss)	ObsID	Exp. (s)	Phase (days)
2021-09-12 1:10:19	14808007	999.7	4.5
2021-09-12 15:17:18	14808007	1322.6	5
2021-09-12 17:04:22	14808007	709.4	5
2021-09-12 21:46:21	14808007	978.9	5
2021-09-13 23:22:18	14808007	946.6	6.5
2021-09-14 10:17:18	14808010	1253.7	7
2021-09-14 12:05:18	14808010	930.9	7
2021-09-14 13:42:19	14808010	930.9	7

Note. Spectra obtained on 2021 September 12 and 2021 September 14 were median combined to increase the S/N, yielding spectra at +5 and +7 days, respectively. The summed spectra are used in Figure 5.

paper, we classify SN 2021yja as an SN IIP, as corroborated by the photometry presented in this section.

The galactic reddening toward SN 2021yja is $E(B - V)_{\text{MW}} = 0.02$ mag (Schlafly & Finkbeiner 2011). We find a small contribution to the extinction from the host galaxy ($E(B - V)_{\text{host}} = 0.05$ mag), such that $E(B - V)_{\text{tot}} = 0.07$ mag (see Section 3.5). The preexplosion site of SN 2021yja is shown in Figure 7 (see Section 3.2). Spectra are dereddened unless specified otherwise. All of the spectra are also corrected for the recession of the host galaxy NGC 1325 using $z = 0.0053$ (NED 2019;²⁰ Smith et al. 2021) unless specified otherwise. A detailed analysis of the optical light curves and spectra is presented by Hosseinzadeh et al. (2022).

3.1. Photometric Comparison with Other SNe

In Figure 8, we compare the *V*-band light curve of SN 2021yja with those of the canonical Type IIL SN 1979C

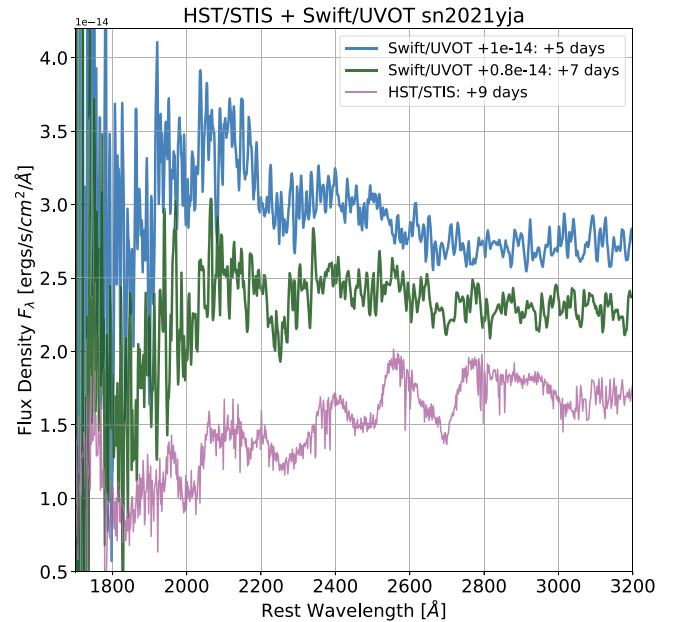


Figure 5. The HST/STIS NUV spectrum of SN 2021yja at +9 days ($S/N \approx 35$) and the median-combined Swift/UVOT spectra of SN 2021yja at +5 and +7 days ($S/N \approx 3$) as described in the text. The Swift/UVOT spectra were arbitrarily shifted for clarity.

(Vaucouleurs et al. 1981) and the Type IIP SNe 1999em (Leonard et al. 2002), 2004et (Maguire et al. 2010), 2005cs (Pastorello et al. 2009), 2012aw (Valenti et al. 2015), 2013ej (Huang et al. 2015), and 2017eaw (Van Dyk et al. 2019). The comparison SNe are well studied and occupy a wide range of light-curve parameters. We apply an extinction correction to each SN. Several studies based on large samples of SN light curves have found that the duration of the *V*-band plateau is shorter for those SNe IIP that exhibit a higher *V*-band peak luminosity (Anderson et al. 2014a; Valenti et al. 2016; de Jaeger et al. 2019). The SN 2021yja displays a long plateau

²⁰ See <https://ned.ipac.caltech.edu/>.

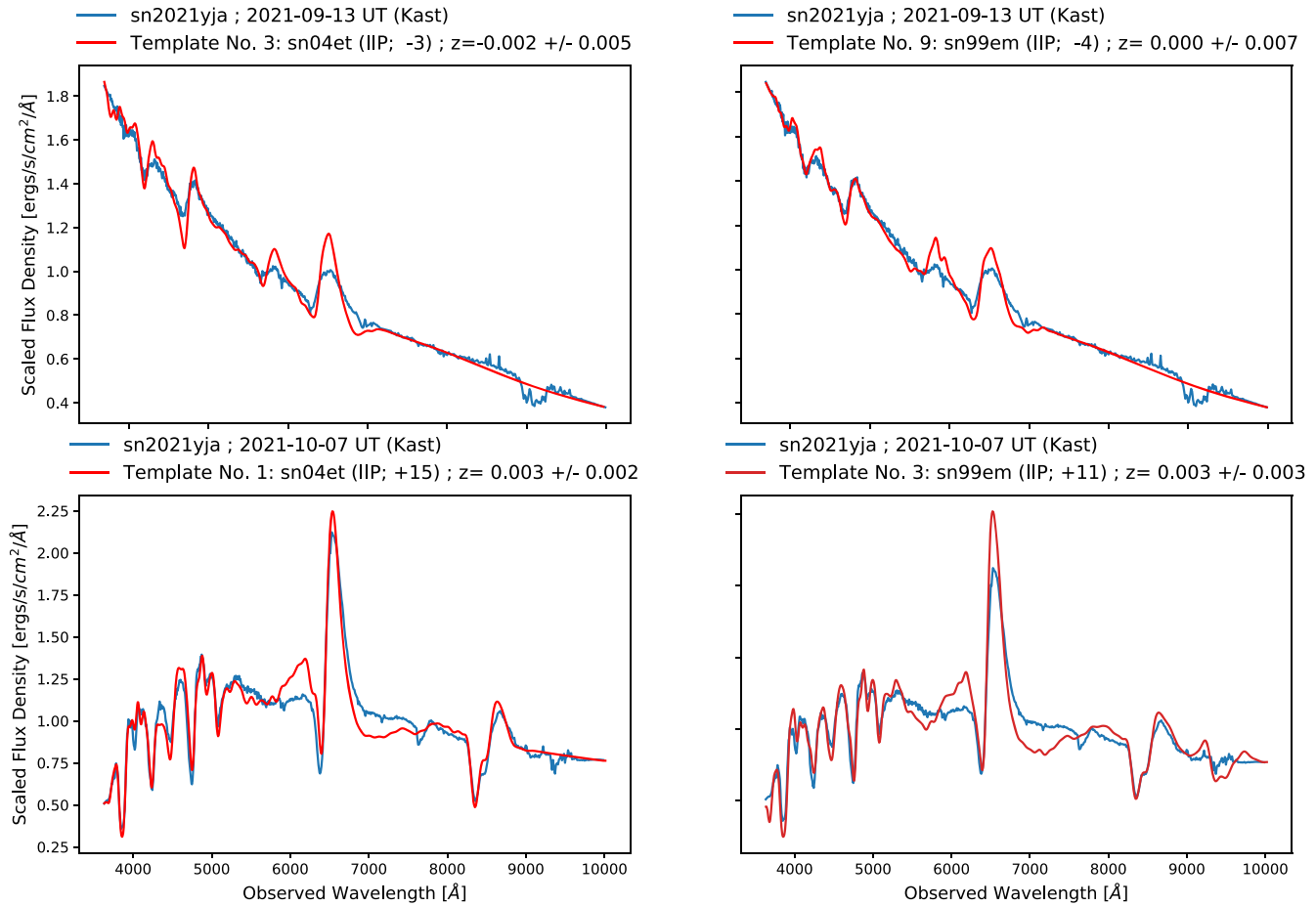


Figure 6. SNID best-fit templates for SN 2021yja on 2021 September 13 (top) and 7 October 2021 (bottom).

phase characteristic of SNe IIP; however, the plateau drop-off is shallower compared to those of the other SNe. The absolute V magnitude, M_V , peaks at nearly -17.5 mag, resembling the average behavior of normal SNe IIP. We note that the object's distance (and therefore derived quantities, such as absolute magnitude) are somewhat uncertain, since it does not have a Cepheid or tip of the red giant branch distance estimate to its host.

The absolute V magnitude at the start of the radioactive tail phase, $M_{\text{tail}} \approx -15.5$, is higher than what is measured in other SNe IIP by Anderson et al. (2014a). The depth of the drop-off is smaller than for the other SNe II in comparison. Valenti et al. (2016) showed that the subluminal explosions tend to have a greater drop-off depth compared to the more typical SNe. The SNe 2021yja and 2004et have a similar behavior (slope) in their postmaximum plateau phase, yet they exhibit noticeably different drop-off slopes and M_{tail} magnitudes. Anderson et al. (2014a) also showed that a brighter tail-phase magnitude correlates with a higher ^{56}Ni mass (see their Figure 33). The long plateau and shallow postplateau drop-off indicate that the explosion of SN 2021yja was more energetic and synthesized more ^{56}Ni compared to the average of SNe IIP such as SN 1999em. This interpretation is also corroborated by the high photospheric velocity at early phases, as inferred from spectroscopic modeling (see Sections 3.6 and 3.5.1).

We estimate the nickel mass from the bolometric luminosity of the exponential tail using the method presented by Hamuy (2003). Using their Equations (1) and (2), our values for the

total extinction $A_V = 3.2 E(B - V) \approx 0.22$ mag, explosion epoch $t_0 = 59,465$, distance $D \approx 21.8$ Mpc, and applying the bolometric correction $BC \approx 0.26$ mag from Hamuy et al. (2001), we estimate the ^{56}Ni mass of SN 2021yja to be $\sim 0.12 M_\odot$ when measured at $t_{\text{tail}} = 59,618.15$ with an apparent KAIT $V_{\text{tail}} \approx 16.94$ mag. Doing the calculation for a few other points on the tail does not appreciably change the results. For SN 1999em, Hamuy (2003) measured a ^{56}Ni mass of $0.04^{+0.027}_{-0.019} M_\odot$. Misra et al. (2007) determined an average ^{56}Ni mass of $0.06 \pm 0.03 M_\odot$ for SN 2004et using the same method at two different points on the tail. Our estimate is consistent with SN 2021yja having a higher bolometric luminosity on the exponential tail compared to SN 1999em and SN 2004et. Compared with the mean ^{56}Ni mass of $0.044 M_\odot$ calculated for Type II SNe ($N = 115$) by Anderson (2019), our ^{56}Ni measurement is greater by more than one standard deviation of their value.

3.2. Search for the RSG Progenitor

We investigated whether the SN progenitor was detected in preexplosion HST images available for the host galaxy in the archive. We found that there were two data sets, both obtained with the Wide Field and Planetary Camera 2 (WFPC2), one set on 1997 March 26 in the F606W filter (600 s total exposure time) and the other on 2001 July 7 in the F450W and F814W filters (460 s in each of the bands). Unfortunately, the latter did not contain the SN site. We attempted to isolate the location of

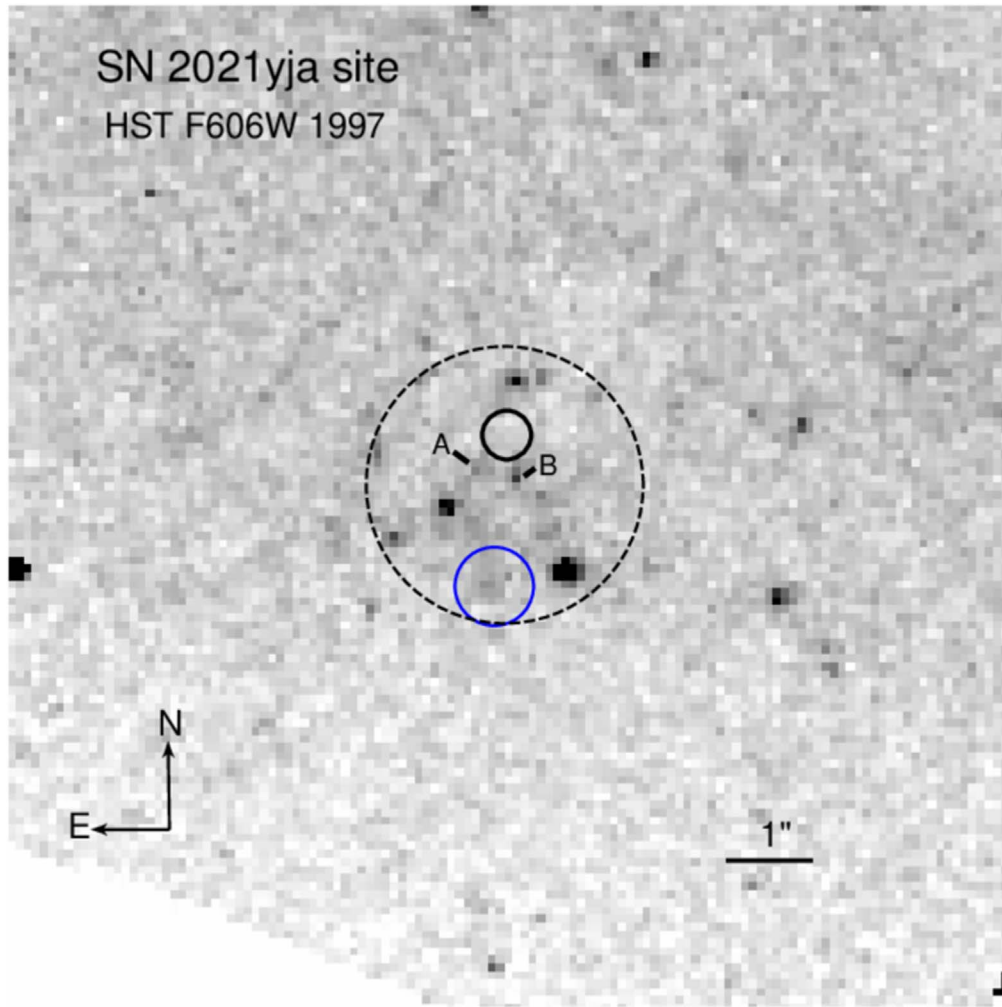


Figure 7. Portion of the preexplosion HST WFPC2 F606W image mosaic, obtained on 1997 March 26, containing the SN 2021yja site. This SN location is indicated with a solid circle, with a radius of the 3σ formal astrometric uncertainty. The dashed circle encompasses the larger overall SN environment, which contains a notable clustering of several detected objects. Two stars that could be considered as progenitor candidates, if the progenitor had not experienced any circumstellar extinction, are indicated as “A” and “B” (see text). We also show with the solid blue circle the approximate position of the SN site as located by Hosseinzadeh et al. (2022). North is up, and east is to the left.

the SN in the former using a combination of two KAIT *R*-band images of the SN, both with comparatively good seeing. We were able to match seven stars in common between the KAIT images and the WFPC2 F606W image mosaic, leading to a 1σ formal uncertainty in the relative astrometry of ~ 1 WFPC2 pixel. The SN location is shown in Figure 7. As can be seen, no source is detected at the SN location to within the astrometric uncertainty.

The SN site is contained within chip 2 of the WFPC2 F606W data set. We employed Dolphot (Dolphin 2016) to perform photometry on that chip. To determine whether the SN progenitor had possibly been detected in the data, we made the following argument. If the progenitor of SN 2021yja were analogous to the progenitor of SN 2017eaw (Van Dyk et al. 2019), then its absolute magnitude should be $M_{F606W} \approx -3.8$ mag. It was shown for the latter progenitor star that substantial circumstellar dust must have been present prior to explosion. If this luminosity is also applied to the SN 2021yja progenitor, then, given our assumptions for the distance and total reddening, we would expect the apparent brightness of the star in the 1997 image to have $m_{F606W} \approx 28.1$ mag. However, we found that the detection threshold was ~ 26.7 mag (formally

at 3σ), so the progenitor would not have been detectable. If the progenitor had not experienced circumstellar extinction, then we might expect the star to have $M_{F606W} \approx -5.9$ mag, for an initial mass of $12 M_{\odot}$, or -6.3 mag for $15 M_{\odot}$ (Stanway & Eldridge 2018). This would mean that the star might be detectable at ~ 26.0 and ~ 25.6 mag, respectively. Two detected stars meeting these respective criteria are labeled in Figure 7 as “A” and “B” and could be considered progenitor candidates. Both stars can be seen outside our formal astrometric uncertainty but are in the general vicinity of the SN location. Clearly, an image of the SN with higher spatial resolution, obtained with HST or adaptive optics (AO) from the ground, is required to pinpoint the SN’s location in the preexplosion data. (We know from Van Dyk et al. 2014 that the SN location determined from low-resolution, ground-based SN imaging can be significantly displaced from that determined via high-resolution imaging.) We attempted to use a coadded mosaic of the three very short (4 s) MIRVIS exposures from our HST/STIS observations to do this; however, unfortunately, no other objects besides the SN were visible in that mosaic. We note that Hosseinzadeh et al. (2022) obtained an AO image and more precisely located the SN site (we show this location in

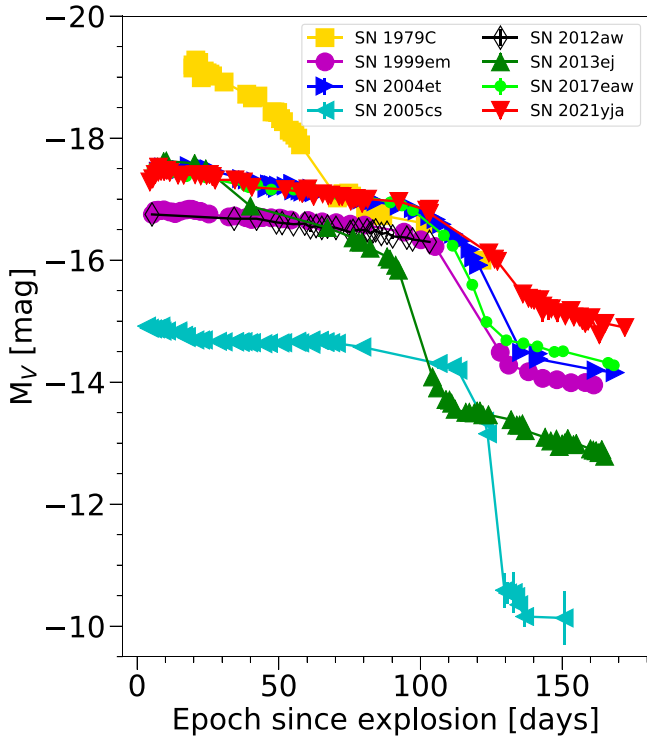


Figure 8. KAIT V-band light curve of SN 2021yja compared with that of other well-studied SNe II: SN 1979C (Vaucoeurs et al. 1981), SN 1999em (Leonard et al. 2002), SN 2004et (Maguire et al. 2010), SN 2005cs (Pastorello et al. 2009), SN 2012aw (de Jaeger et al. 2019), SN 2013ej (Huang et al. 2015), and SN 2017eaw (Van Dyk et al. 2019).

Figure 7), although they were unable to identify a progenitor candidate.

3.3. The UV Spectrum

It has been suggested that SNe IIP show remarkable similarities in their UV spectra (2000–3500 Å) at ~10 days after the explosion (Gal-Yam et al. 2008; Bufano et al. 2009; Dhungana et al. 2016). Here we investigate the early UV spectroscopic properties of SN 2021yja and test this claim through a thorough comparison between our observations and those of other SNe II that have early-time UV spectra.

In Figure 2, we present the HST/STIS UV-optical spectra of SN 2021yja obtained on days +9, +14, and +21. A comparison between the earliest HST/STIS spectrum and the Swift/UVOT spectra at days +5 and +7 is given in Figure 5. We identify prominent blueshifted hydrogen Balmer lines and the characteristic Mg II λ 2798 absorption line in the HST/STIS spectra of SN 2021yja. These features are also generally present in other SNe II, such as SNe 1999em, 2005cs, 2005ay, and 2012aw (Baron et al. 2000; Brown et al. 2007; Gal-Yam et al. 2008; Bufano et al. 2009; Bayless et al. 2013). The UV spectrum blueward of 3000 Å is dominated by superposed Fe II and Fe III lines, causing a significant amount of line blanketing (Dessart & Hillier 2005b). The emission peaks at these wavelengths correspond to regions of reduced line blanketing (Brown et al. 2007). By day 21, we observe a relatively smooth and featureless continuum in the 2000–3000 Å region as line-blanketing effects strengthen in the cooling ejecta.

Figure 9 compares the UV spectrum of SN 2021yja at +14 days with that of several other SNe II observed at similar

phases, including the Type IIP SNe 1999em, 2005ay, and 2012aw (Baron et al. 2000; Gal-Yam et al. 2008; Bayless et al. 2013); the transitional object SN 2013ej between Types IIP and IIL (Dhungana et al. 2016); and the Type IIL SN 2013df (Ben-Ami et al. 2015). We include the last of these to demonstrate the effect of extreme CSM interaction on the UV flux. In contrast to the previous suggestions of homogeneity, we see some similarities but also clear differences among the Type IIP UV spectra. For example, SN 1999em shows a strong peak near 3000 Å that is not seen in SN 2021yja. There are substantial differences among SNe 2012aw and 2013ej as well, primarily at wavelengths redder than 2800 Å. Nagao et al. (2021) found that SN 2013ej shows evidence for weak-to-moderate CSM interaction, which is consistent with the shallower P Cygni trough and smoother UV flux. The SN IIL 2013df appears to be quite different, with a prominent peak near 2700 Å, where the other objects show a dip, and a more featureless continuum below 2600 Å.

We attribute the variations in the UV flux shape to a combination of factors, possibly including the epoch uncertainty and differences in metallicity, reddening, and preexplosion behavior.

The Mg II λ 2798 line is among the most well-studied features in the UV spectra of SNe II. Its shape has been used to infer the explosion properties of SNe II (see Sections 3.5.1 and 3.6). At +9 and +14 days, the Mg II λ 2798 feature in SN 2021yja displays a prominent P Cygni profile. By contrast, only a weak absorption component at ~2700 Å can be seen across the Mg II λ 2798 line observed at +5 and +7 days (see Figure 5). The Mg II absorption changes shape quite dramatically between +9 and +14 days as it develops a boxy trough (Figure 12), compared to H β (Figure 13) and H α (Figure 14). By day +21, the P Cygni profile overlaps with a series of metal lines and therefore appears less prominent. The broad P Cygni feature is indicative of Mg II formation close to the photosphere (see Section 3.7). This is in stark contrast to SN 2013df, which shows an asymmetric and strongly blueshifted Mg II line, suggesting that its formation is far above the photosphere and in the CSM (Ben-Ami et al. 2015).

We also identify the Fe II line at 2900 Å, commonly observed in the other SNe II. Of note is the line blanketing by Ti II and Ni II around 3000 and 2500 Å, respectively. These lines of singly ionized species were also observed in SN 2005cs and discussed by Bufano et al. (2009).

The UV spectra of SN 2021yja are also distinct from those of peculiar Type II SNe such as SN 1987A, which displays a sharp cutoff in the UV flux below 3000 Å (Kirshner et al. 1987; Pun et al. 1995). There are also notable differences between the SNe IIP and the interacting SN IIL 2013df, primarily in the latter’s blueshifted Mg II P Cygni feature and relatively smooth spectrum below 2600 Å (Ben-Ami et al. 2015).

3.4. The Optical Spectrum

The optical spectral evolution of SN 2021yja is presented in Figure 3. We also compare the +6 day Kast spectrum to that of other well-studied SNe in Figure 15, showing that the early optical spectrum fits within the framework. A total of 12 spectra were obtained by Kast and HST, spanning from +4 to +121 days.

Within the first ~10 days after the SN explosion, the optical spectra of SN 2021yja are characterized by a series of broad Balmer lines superimposed on a hot, featureless continuum. We

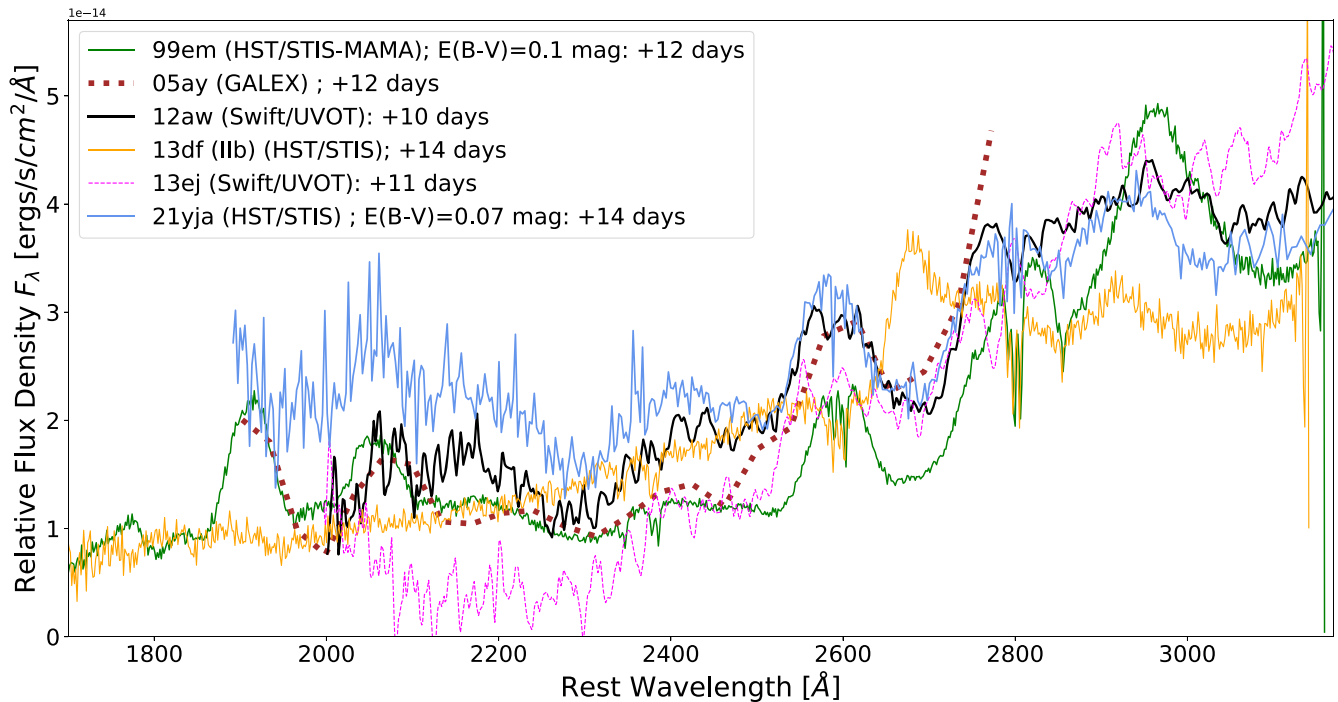


Figure 9. The HST/STIS UV spectrum of SN 2021yja at +14 days compared with the well-studied Type IIP SNe 1999em (Baron et al. 2000), 2005ay (Gal-Yam et al. 2008), and 2012aw (Bayless et al. 2013; Rowe et al. 2022, in preparation); Type IIP/L SN 2013ej (Dhungana et al. 2016); and the Type IIB SN 2013df (Ben-Ami et al. 2015) observed at similar phases. All wavelength scales were corrected to the rest frame according to their host’s redshift. All spectra were also dereddened assuming an $R_V = 3.1$ extinction law.

associate the weak feature around 5800 Å at +9 days with the He I $\lambda 5876$ line. After $\sim +30$ days, the O I $\lambda 7774$ and Ca II NIR triplet became progressively dominant at red wavelengths, corresponding to the plateau phase of the SN. The temporal evolution of the PCygni profile across the H α feature of SN 2021yja appears to be similar to those observed from other SNe IIP (Gutiérrez et al. 2017). We do not observe the strong Si II $\lambda 6355$ line that was reported for the transitional Type IIP–IIL SN 2013ej at ~ 2 –3 weeks (Valenti et al. 2014). The blue part of the optical spectra after day +30 is characterized by a series of features of intermediate mass and heavy elements such as Na, Ca, and Fe. The PCygni profiles are also becoming more pronounced.

We observe a change in the location of the H α emission peak over time. The evolution of the H α emission line is plotted in Figure 16 for two HST and four Kast epochs. The HST spectrum at +14 days shows a blueshift of nearly 4000 km s $^{-1}$. The blueshift of the emission component decreases roughly linearly with time, reaching a velocity of ~ 1000 km s $^{-1}$ by day +61. This blueshifted emission peak (a few thousand kilometers per second) is consistent with a steep density profile and commonly observed in other SNe IIP (Dessart & Hillier 2005b; Anderson et al. 2014b; see Section 3.5.2).

A notch forms in the left wing of the H α absorption at +121 days. This feature has been interpreted as evidence for high-velocity H α absorption caused by CSM interaction (Chugai et al. 2007). However, we do not observe the late-time asymmetries in the H α emission peak that were present in the spectrum of SN 2013ej at around 129 days, which were interpreted as evidence for CSM interaction; see Dhungana et al. (2016).

Although SNe IIL are spectroscopically similar, they show characteristically flatter Balmer lines compared to SNe IIP, likely

owing to a lack of hydrogen in deeper and slower-expanding layers of ejecta or interaction with the CSM (Hillier & Dessart 2019).

3.5. Modeling with TARDIS

Type II SNe have been previously modeled using sophisticated radiative transfer codes, notably by Baron et al. (2004) using PHOENIX, as well as by Dessart & Hillier (2006) and Dessart et al. (2008) with CMFGEN. For spectral modeling, we use a modified version of the Monte Carlo radiative transfer code TARDIS developed for the analysis of SNe II (Kerzendorf & Sim 2014; Vogl et al. 2019). The code treats the excitation and ionization of hydrogen in non-local thermodynamic equilibrium (NLTE). The level populations of other elements are generally calculated with a simplified NLTE treatment—the nebular approximation of Mazzali & Lucy (1993)—to reduce computational costs. This potentially limits the accuracy for estimates of species ionization and thus the metallicity.

In our analysis of the HST spectra, we assume a power-law density profile and a homogeneous composition. The models differ in the steepness of the density profile n , temperature, velocity, metallicity, and time since explosion. In addition to the SN parameters, we vary the value for the host extinction, $E(B - V)_{\text{host}}$. We use a machine-learning emulator, trained on a large grid of TARDIS simulations, to fit the models to the data as in Vogl et al. (2020). The emulator generates synthetic spectra much faster for new parameter combinations than TARDIS, allowing us to find the best-fitting parameters through χ^2 minimization. Only the third epoch falls within the parameter space of the emulator from Vogl et al. (2020). We use a new set of models that extends to higher temperatures and velocities and steeper density profiles for the first two epochs. Compared

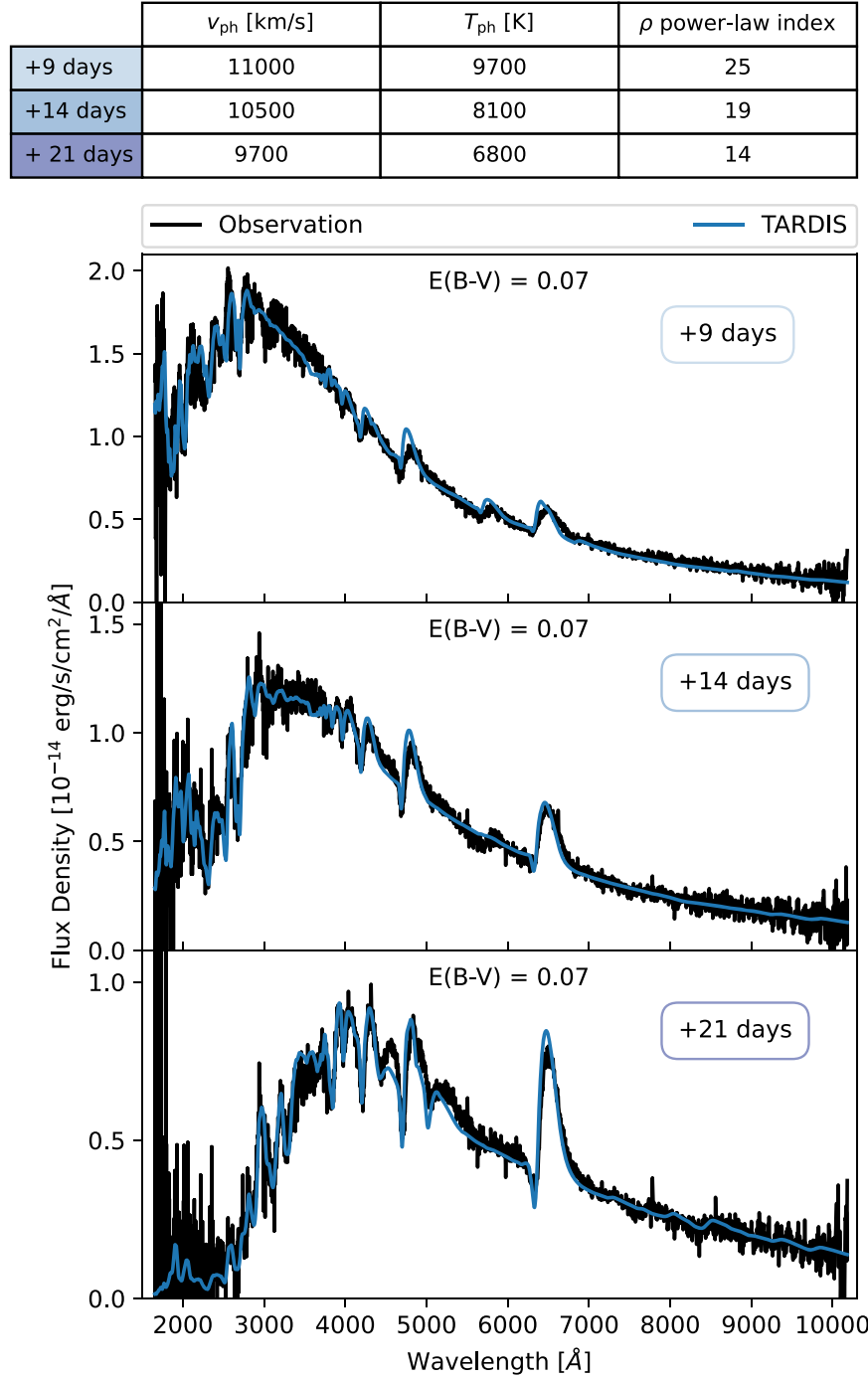


Figure 10. TARDIS fits to the HST STIS UV-optical spectra of SN 2021yja at +9 (top), +14 (middle), and +21 days (bottom). The best-fit parameters are presented above the top panel.

to the older simulations, we treat helium in NLTE to produce more accurate spectra at high temperatures.

Our TARDIS fits for the three HST observations are shown in Figure 10. The plot includes a table with estimates of the key fit parameters: the photospheric velocity v_{ph} , the photospheric temperature T_{ph} (i.e., the gas temperature at the photosphere), and the power-law index of the density profile n . The fits indicate some additional host galaxy extinction $E(B - V)_{\text{total}} \approx 0.07$ mag and a subsolar metallicity. Given the uncertainties in the modeling (e.g., the approximate NLTE treatment of metal species) and a certain degree of degeneracy between metallicity, temperature,

and extinction, we provide only a qualitative estimate for the metallicity.

3.5.1. Evolution of the Photospheric Temperature and Velocity

In Figure 11, we plot the time-series evolution of T_{ph} and v_{ph} for SNe 1999em, 2005cs, 2006bp, and 2021yja. We use the inferred values from Dessart et al. (2008, hereafter D08), Bose et al. (2013), and Vogl et al. (2019, hereafter V19) in our comparison. The high photospheric velocities found for SN 2021yja are comparable to those of SN 2006bp (D08).

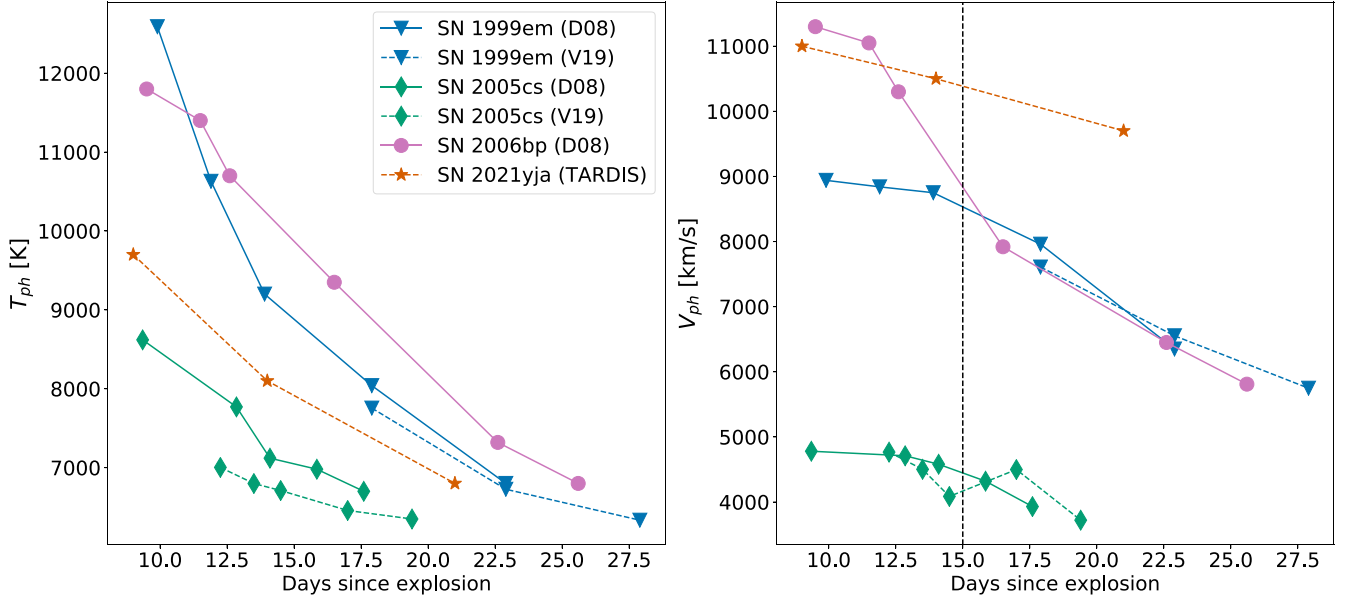


Figure 11. Photospheric temperature T_{ph} (left) and photospheric velocity v_{ph} (right) evolution of SN 2021yja obtained from the TARDIS fit to the three epochs of HST/STIS spectra compared to that of SNe 1999em, 2005cs, and 2006bp (D08; V19). The vertical dashed line indicates the velocity at +15 days, v_{d15} , for comparison purposes.

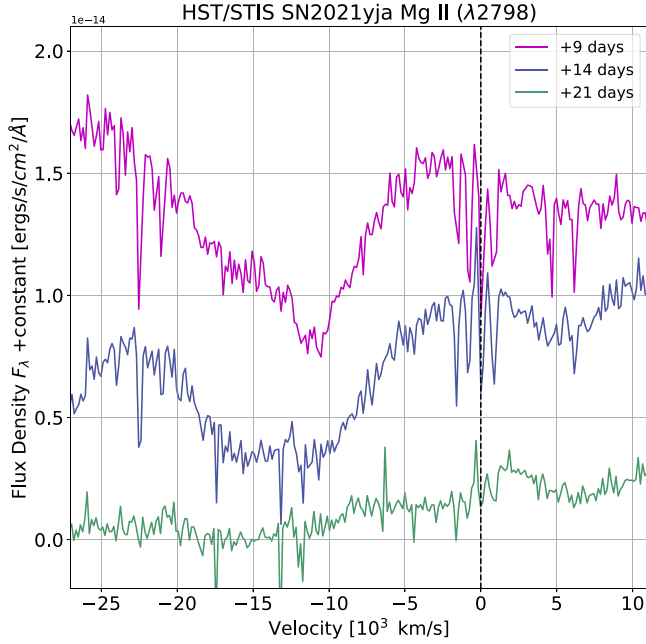


Figure 12. The Mg II line evolution for three HST epochs, dereddened with $E(B - V) = 0.07$ mag assuming $R_V = 3.1$.

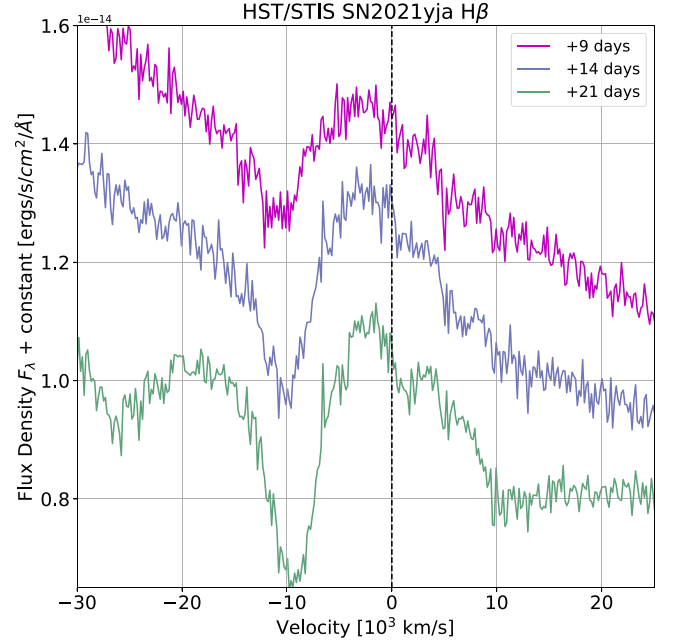


Figure 13. The H β line evolution for three HST epochs, dereddened with $E(B - V) = 0.07$ mag assuming $R_V = 3.1$.

The photosphere cools as the ejecta expand adiabatically. The inferred T_{ph} for SN 2021yja is consistent with the other SNe IIP in our comparison. In our range of observations, we observe that T_{ph} declines roughly linearly with time. The SNe IIP are shown to slow down their rate of cooling as they approach a temperature of ~ 6000 K, indicating the onset of the plateau phase. The photospheric temperature is roughly similar to that of SN 2012aw and SN 2013ej (not plotted here), while the subluminous SN 2005cs has a T_{ph} smaller by a factor of 2.

Faran et al. (2014) found that the photospheric velocity is higher for SNe IIL than for SNe IIP. In the literature, the Fe II

absorption minimum (e.g., $\lambda 5169$) is used as a reasonable estimate for the photospheric velocity for SNe IIP (Hamuy et al. 2001; Leonard et al. 2002; Dessart & Hillier 2005b), whereas in this work and that of D08 and V19, the photospheric velocity is obtained using radiative transfer modeling. We infer a remarkably high photospheric velocity for SN 2021yja, starting at $11,000 \text{ km s}^{-1}$ on day +9 and slowly decreasing to $10,500 \text{ km s}^{-1}$ on day +14 and 9700 km s^{-1} on day +21. We show in our comparison to other SNe in Figure 11 that SN 2021yja has a relatively high V_{ph} , well above that of SN 1999em and SN 2005cs, even exceeding that of SN 2006bp at later epochs. This suggests a high explosion energy compared to a typical SN IIP (see Section 3.6).

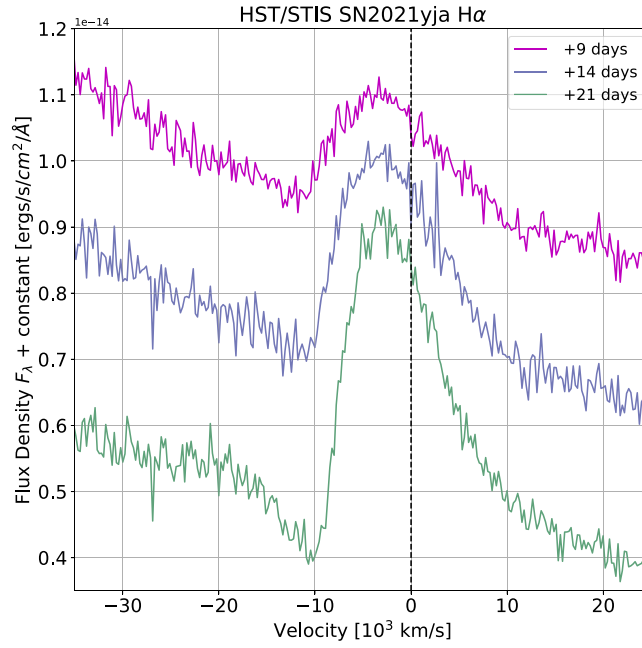


Figure 14. The H α line evolution for three HST epochs, dereddened with $E(B - V) = 0.07$ mag assuming $R_V = 3.1$.

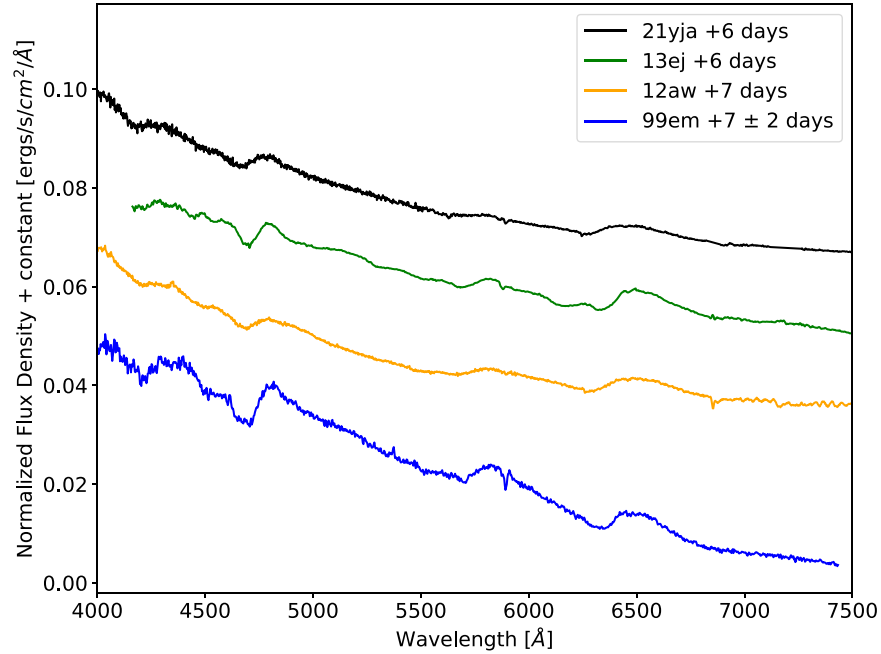


Figure 15. Comparison of SN 2021yja optical spectrum at +6 days to that of other SNe IIP.

3.5.2. Density Profile and P Cygni Blueshift

The radial density profile of SNe II can be modeled by a power law, $\rho = \rho_0(r/r_0)^{-n}$, where ρ_0 represents the density at a corresponding characteristic radius r_0 , and n denotes the index of the power law. Early observations of SNe II exhibit a steep density decrease with radius that gradually flattens with time. For SNe IIP, the typical value for n during the first 2 weeks after explosion can be upward of 20, dropping down to roughly 10 during the photospheric phase (Dessart et al. 2008; Vogl et al. 2019). For SN 2021yja, we find that the temporal evolution of n is consistent with the literature. The inferred values for n are shown in the rightmost column of Figure 10.

A consequence of the varying density profile is the temporal blueshift of the H α emission peak (Anderson et al. 2014b). We observe this effect in Figure 16, with the H α emission peak weakening in its blueshift as the density profile power-law index falls from $n = 25$ on day +9 to $n = 14$ on day +21. Other effects of changing n are discussed by Dessart & Hillier (2005b) but are beyond the scope of this work.

3.6. Energetics

The photospheric velocity serves as a useful tracer of SN kinematics. The principle of such a method—in particular, a relationship between the kinetic energy of the SN ejecta and the

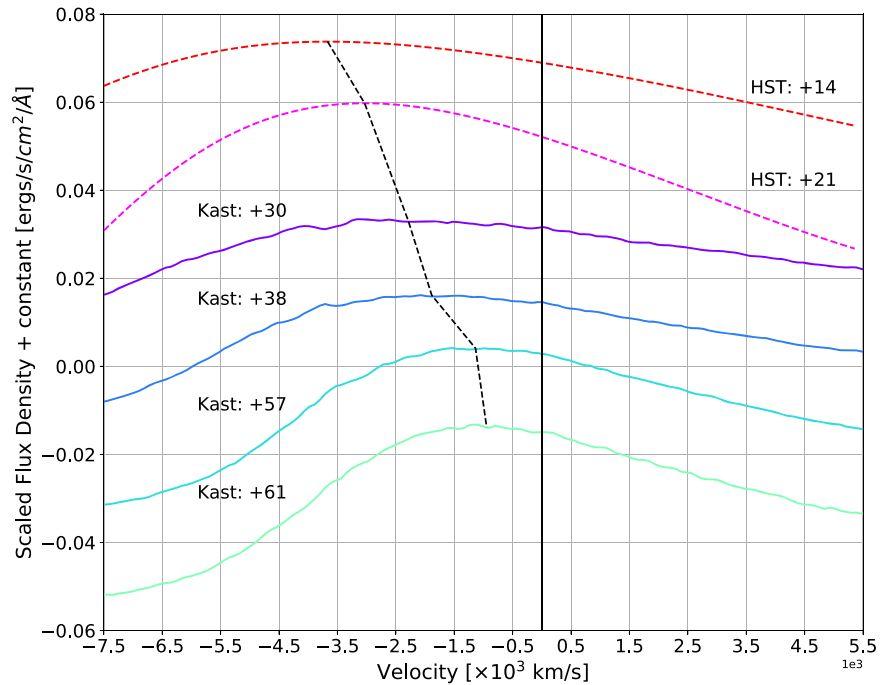


Figure 16. Evolution of the $H\alpha$ profile of SN 2021yja from days +14 to +61 presented in velocity space. Color-coded dashed curves present high-order polynomial fits to the HST spectra, which are used to estimate the location of the emission peaks. The black dashed curve traces the shift of the $H\alpha$ emission peak. All spectra are corrected for the redshift of the host galaxy and the extinctions from the host and the Milky Way. The spectra were scaled arbitrarily for clarity.

photospheric velocity at 15 days after shock breakout, v_{d15} —has been discussed by Dessart et al. (2010; see their Figure 4). Explosions with an energy of 1 foe (10^{51} erg) have $v_{d15} < 9000 \text{ km s}^{-1}$, whereas explosions with an energy of 3 foe have $v_{d15} > 12,000 \text{ km s}^{-1}$. Although we do not have any data for the +15 day phase, we can approximate v_{d15} by using the photospheric velocity at +14 days. The SN 2021yja appears to be a high-energy/velocity clone of SN 1999em and closer to SN 2012aw (see Bose et al. 2013).

Based on the TARDIS modeling from days +9 to +21, we estimate that SN 2021yja has $v_{d15} \approx 10,300 \text{ km s}^{-1}$, yielding an asymptotic ejecta kinetic energy of 1–3 foe, whereas SN 1999em has ~ 1 foe, and SN 2005cs has ~ 0.1 – 0.3 foe. The SN 2021yja has an initial explosion energy higher than typical SNe IIP, similar to SN 2006bp, considering that both SNe exhibit comparable photospheric velocity evolution at early times.

3.7. Origin of the UV and Optical Flux

In this section, we discuss whether the MUV and optical flux originate from the photosphere or CSM interaction. The Mg II $\lambda 2800$ line has been used to determine the origin of the UV flux for a small sample of SNe II. For example, Brown et al. (2007) showed that the Mg II $\lambda 2798$ line in the SN 2005cs Swift/UVOT spectrum has a broad P Cygni profile with a velocity comparable to v_{ph} , suggesting that the UV flux originates in the photosphere, not CSM. On the other hand, Pun et al. (1995) found that the highly interacting Type IIL SN 1979C had a narrower Mg II line in addition to a relatively smooth UV spectrum compared with SNe IIP. A smooth UV spectrum that does not show any obvious broad absorption features within a few weeks after the explosion is expected for SNe that interact with thick circumstellar envelopes (Pun et al. 1995). For example, the CSM-interacting Type IIB SN 2013df shown in Figure 9 has a smooth MUV continuum, weak absorption lines, and a blueshifted Mg II

emission peak. Other examples include Type IIB SN 1993J, which also had a smooth UV spectrum lacking any broad absorption features, similar to SNe IILs 1979C and 1980K (Jeffery et al. 1994).

The detection of X-rays in the first weeks after the explosion has been used to argue for CSM interaction in SNe II. Immler et al. (2007) and Dessart et al. (2008) showed that in the case of SN 2006bp, although X-rays were observed for up to 12 days after explosion, suggesting that interaction between the ejecta and the CSM occurred, there was no sizable contribution to the UV or optical flux. The X-ray emission suggesting CSM interaction has also been observed for more recent events, such as SN 2012aw (Immler & Brown 2012) and SN 2013ej (Margutti et al. 2013). The modeling fits for SN 2021yja manage to reproduce both the UV and optical spectrum without needing to take into account an additional heating source, such as an ejecta–CSM interaction. In other words, the CSM does not provide a sizable effect on the flux, unlike what is observed for the interacting SN IIB 2013df (Ben-Ami et al. 2015; see their Figure 5). It is therefore unlikely that the CSM is a significant contributor to the high continuum polarization of SN 2021yja observed during the photospheric phase (Vasylyev et al. 2022, in preparation). These conclusions support a photospheric origin for the UV flux.

Fransson et al. (1984) suggested that the UV flux below 1500 Å , which primarily contains emission lines of highly ionized species (N V, N III, Si V), may originate from the SN ejecta interacting with the preexisting CSM. However, the wavelength coverage of the SN 2021yja observations does not capture this parameter space; thus, we limit our discussion to the origin of the NUV-to-MUV flux, 1700 – 3200 Å .

The Mg II velocity widths of SN 2021yja are comparable to those of $H\beta$, suggesting that the UV flux originates close to the photosphere, unlike in SNe highly interacting with CSM (see Figures 12 and 13). In summary, we do not see strong evidence for the existence of CSM that would significantly affect the UV and optical flux.

4. Conclusions

We present multiepoch HST/STIS and Swift/UVOT UV spectra of the young, nearby Type IIP SN 2021yja. Kast optical spectra are also given for six epochs of the photospheric phase up until the plateau drop-off. We compare the UV/optical spectrum of SN 2021yja to that of previously studied SNe with high-S/N data at similar epochs. The SN 2021yja fits well within the framework of other SNe IIP, primarily in the shape and location of the strong Mg II P Cygni profile.

Using the TARDIS code, we infer useful parameters of the explosion, including photospheric velocity, photospheric temperature, density profile power-law index, and metallicity. We qualitatively show that the luminous tail phase and high photospheric velocity suggest that SN 2021yja underwent a more energetic explosion compared to SN 1999em-like SNe II, also producing more ^{56}Ni . We do not find evidence from our modeling for a significant contribution to the UV flux by CSM interaction. This and the high-energy nature of the explosion suggest an aspherical explosion, given that SN 2021yja was found to have high continuum polarization ($p \approx 0.8\%$) during the photospheric phase (Vasylyev et al. 2022, in preparation).

This research was funded by HST grants AR-14259 and GO-16178 from the Space Telescope Science Institute (STScI), which is operated by the Association of Universities for Research in Astronomy (AURA), Inc., under NASA contract NAS5-26555. Additional generous financial support was provided to A.V.F.'s supernova group at UC Berkeley by Steven Nelson, Landon Noll, Sunil Nagaraj, Sandy Otellini, Gary and Cynthia Bengier, Clark and Sharon Winslow, Sanford Robertson, the Christopher R. Redlich Fund, and the Miller Institute for Basic Research in Science (in which A.V.F. was a Miller Senior Fellow). The research of Y.Y. is supported through the Bengier-Winslow-Robertson Postdoctoral Fellowship.

A major upgrade of the Kast spectrograph on the Shane 3 m telescope at Lick Observatory, led by Brad Holden, was made possible through gifts from the Heising-Simons Foundation, William and Marina Kast, and the University of California Observatories. KAIT and its ongoing operation were made possible by donations from Sun Microsystems, Inc., the Hewlett-Packard Company, AutoScope Corporation, Lick Observatory, the National Science Foundation, the University of California, the Sylvia & Jim Katzman Foundation, and the TABASGO Foundation. Research at Lick Observatory is partially supported by a generous gift from Google. We thank the staffs at STScI (especially Weston Eck and Svea Hernandez) and Lick Observatory for assistance with the observations. UC Berkeley undergraduates Ivan Altunin, Raphael Baer-Way, Michael May, Vidhi Chander, and Evelyn Liu obtained some of the Lick/Nickel data.















M.W. acknowledges support from the NASA Future Investigators in NASA Earth and Space Science and Technology grant (80NSSC21K1849) and support from the Thomas J. Moore Fellowship at New York University. M.M.'s research is supported in part by Swift GI program 1619152 (NASA grant 80NSSC21K0280), TESS GI program G03267 (NASA grant 80NSSC21K0240), and a grant from the New York University Research Challenge Fund Program.

This research made use of TARDIS, a community-developed software package for spectral synthesis in supernovae (Kerzendorf & Sim 2014; Kerzendorf et al. 2022). The development of TARDIS received support from GitHub, the Google Summer

of Code initiative, and ESA's Summer of Code in Space program. TARDIS is a fiscally sponsored project of NumFOCUS. TARDIS makes extensive use of Astropy and Pyne.

Software: Astropy (Astropy Collaboration et al. 2013, 2018), TARDIS (Kerzendorf & Sim 2014; Vogl et al. 2019), uvotpy (Kuin 2014), DAOPHOT (Stetson 1987), IDL Astronomy user's library (Landsman 1993), SOUSA pipeline (Brown et al. 2014), Pyne (Scopatz et al. 2012).

ORCID iDs

Sergiy S. Vasylyev  <https://orcid.org/0000-0002-4951-8762>
 Alexei V. Filippenko  <https://orcid.org/0000-0003-3460-0103>
 Christian Vogl  <https://orcid.org/0000-0002-7941-5692>
 Thomas G. Brink  <https://orcid.org/0000-0001-5955-2502>
 Peter J. Brown  <https://orcid.org/0000-0001-6272-5507>
 Thomas de Jaeger  <https://orcid.org/0000-0001-6069-1139>
 Thomas Matheson  <https://orcid.org/0000-0001-6685-0479>
 Avishay Gal-Yam  <https://orcid.org/0000-0002-3653-5598>
 Paolo A. Mazzali  <https://orcid.org/0000-0001-6876-8284>
 Maryam Modjaz  <https://orcid.org/0000-0001-7132-0333>
 Kishore C. Patra  <https://orcid.org/0000-0002-1092-6806>
 Micalyn Rowe  <https://orcid.org/0000-0001-9710-4217>
 Nathan Smith  <https://orcid.org/0000-0001-5510-2424>
 Schuyler D. Van Dyk  <https://orcid.org/0000-0001-9038-9950>
 Marc Williamson  <https://orcid.org/0000-0003-2544-4516>
 WeiKang Zheng  <https://orcid.org/0000-0002-2636-6508>
 Ori D. Fox  <https://orcid.org/0000-0003-2238-1572>
 Elinor L. Gates  <https://orcid.org/0000-0002-3739-0423>
 R. Michael Rich  <https://orcid.org/0000-0003-0427-8387>

References

- Anderson, J. P. 2019, *A&A*, **628**, A7
 Anderson, J. P., González-Gaitán, S., Hamuy, M., et al. 2014a, *ApJ*, **786**, 67
 Anderson, J. P., Dessart, L., Gutierrez, C. P., et al. 2014b, *MNRAS*, **441**, 671
 Astropy Collaboration, Robitaille, T. P., Tollerud, J., et al. 2013, *A&A*, **558**, A33
 Astropy Collaboration, Price-Whelan, A. M., Sipőcz, B. M., et al. 2018, *AJ*, **156**, 123
 Baron, E., Nugent, P. E., Branch, D., & Hauschildt, P. H. 2004, *ApJL*, **616**, L91
 Baron, E., Branch, D., Hauschildt, P. H., et al. 2000, *ApJ*, **545**, 444
 Bayless, A. J., Pritchard, T. A., Roming, P. W. A., et al. 2013, *ApJL*, **764**, L13
 Ben-Ami, S., Hachinger, S., Gal-Yam, A., et al. 2015, *ApJ*, **803**, 40
 Blondin, S., & Tonry, J. L. 2007, *ApJ*, **666**, 1024
 Bose, S., Kumar, B., Sutar, F., et al. 2013, *MNRAS*, **433**, 1871
 Brown, P. J., Breeveld, A. A., Holland, S., Kuin, P., & Pritchard, T. 2014, *ApSS*, **354**, 89
 Brown, P. J., Dessart, L., Holland, S. T., et al. 2007, *ApJ*, **659**, 1488
 Bufano, F., Immler, S., Turatto, M., et al. 2009, *ApJ*, **700**, 1456
 Chugai, N. N., Chevalier, R. A., & Utrobin, V. P. 2007, *ApJ*, **662**, 1136
 Davies, B., & Beasor, E. R. 2020, *MNRAS*, **493**, 468
 de Jaeger, T., Zheng, W., Stahl, B. E., et al. 2019, *MNRAS*, **490**, 2799
 Dessart, L., & Hillier, D. J. 2005a, *A&A*, **439**, 671
 Dessart, L., & Hillier, D. J. 2005b, *A&A*, **437**, 667
 Dessart, L., & Hillier, D. J. 2006, *A&A*, **447**, 691
 Dessart, L., Livne, E., & Waldman, R. 2010, *MNRAS*, **408**, 827
 Dessart, L., Blondin, S., Brown, P. J., et al. 2008, *ApJ*, **675**, 644
 Dhungana, G., Kehoe, R., Vinko, J., et al. 2016, *ApJ*, **822**, 6
 Dolphin, A. 2016, DOLPHOT: Stellar photometry, Astrophysics Source Code Library, ascl:1608.013
 Faran, T., Poznanski, D., Filippenko, A. V., et al. 2014, *MNRAS*, **442**, 844
 Filippenko, A. V. 1997, *ARA&A*, **35**, 309
 Filippenko, A. V., Li, W. D., Treffers, R. R., & Modjaz, M. 2001, in *Small Telescope Astronomy on Global Scales*, ASP Conf. Ser. 246 (San Francisco, CA: ASP), 121

- Fransson, C., Benvenuti, P., Gordon, C., et al. 1984, *A&A*, **132**, 1
- Gal-Yam, A., Bufano, F., Barlow, T. A., et al. 2008, *ApJL*, **685**, L117
- Gehrels, N., Chincarini, G., Giommi, P., et al. 2004, *ApJ*, **611**, 1005
- Gutiérrez, C. P., Anderson, J. P., Hamuy, M., et al. 2017, *ApJ*, **850**, 89
- Hamuy, M. 2003, *ApJ*, **582**, 905
- Hamuy, M., Pinto, P. A., Maza, J., et al. 2001, *ApJ*, **558**, 615
- Hillier, D. J., & Dessart, L. 2019, *A&A*, **631**, A8
- Hiramatsu, D., Burke, J., Arcavi, I., et al. 2019, TNS Classification Report No. 2019-745, IAU Supernova Working Group, <https://www.wis-tns.org/object/2019ewu/classification-cert>
- Hosseinzadeh, G., Kilpatrick, C. D., Dong, Y., et al. 2022, arXiv:2203.08155
- Huang, F., Wang, X., Zhang, J., et al. 2015, *ApJ*, **807**, 59
- Immler, S., & Brown, P. J. 2012, *ATel*, **3995**, 1
- Immler, S., Brown, P. J., Milne, P., et al. 2007, *ApJ*, **664**, 435
- Jeffery, D. J., Kirshner, R. P., Challis, P. M., et al. 1994, *ApJL*, **421**, L27
- Kerzendorf, W., Sim, S., Vogl, C., et al. 2022, tardis-sn/tardis: TARDIS v2022.2.27, Zenodo, doi:10.5281/zenodo.6299948
- Kerzendorf, W. E., & Sim, S. A. 2014, *MNRAS*, **440**, 387
- Kilpatrick, C. D. 2021, TNSAN, **236**, 1
- Kirshner, R. P., & Kwan, J. 1974, *ApJ*, **193**, 27
- Kirshner, R. P., Sonneborn, G., Crenshaw, D. M., & Nassiopoulos, G. E. 1987, *ApJ*, **320**, 602
- Kuin, N. P. M., Landsman, W., Breeveld, A. A., et al. 2015, *MNRAS*, **449**, 2514
- Kuin, P. 2014, UVOTPY: Swift UVOT grism data reduction, Astrophysics Source Code Library, ascl:1410.004
- Landolt, A. U. 1992, *AJ*, **104**, 340
- Landsman, W. B. 1993, in *Astronomical Data Analysis Software and Systems II*, A.S.P. Conf. Ser. 52, ed. R. J. Hanisch et al. (San Francisco, CA: ASP), **246**
- Leonard, D. C., Filippenko, A. V., Gates, E. L., et al. 2002, *PASP*, **114**, 35
- Li, W., Leaman, J., Chornock, R., et al. 2011, *MNRAS*, **412**, 1441
- Maguire, K., Di Carlo, E., Smartt, S. J., et al. 2010, *MNRAS*, **404**, 981
- Margutti, R., Chakraborti, S., Brown, P. J., & Sokolovsky, K. 2013, *ATel*, **5243**, 1
- Mazzali, P. A. 2000, *A&A*, **363**, 705
- Mazzali, P. A., & Lucy, L. B. 1993, *A&A*, **279**, 447
- Miller, J. S., Robinson, L. B., & Goodrich, R. W. 1988, in *Instrumentation for Ground-Based Optical Astronomy*, ed. L. B. Robinson (New York, NY: Springer), **157**
- Miller, J. S., & Stone, R. P. S. 1993, Lick Obs. Tech. Rep. No. 66, Univ. California
- Misra, K., Pooley, D., Chandra, P., et al. 2007, *MNRAS*, **381**, 280
- Nagao, T., Patat, F., Taubenberger, S., et al. 2021, *MNRAS*, **505**, 3664
- NASA/IPAC Extragalactic Database (NED) 2019, NASA/IPAC Extragalactic Database (NED), IPAC, doi:10.26132/NED1
- Panagia, N., Vettolani, G., Boksenberg, A., et al. 1980, *MNRAS*, **192**, 861
- Pastorello, A., Valenti, S., Zampieri, L., et al. 2009, *MNRAS*, **394**, 2266
- Pellegrino, C., Burke, J., Hiramatsu, D., et al. 2021, Global SN Project Transient Classification Report for 2021-09-09
- Prichard, L., Welty, D., & Jones, A. 2022, STIS Instrument Handbook for Cycle 30 (Baltimore: STScI)
- Pun, C. S. J., Kirshner, R. P., Sonneborn, G., et al. 1995, *ApJS*, **99**, 223
- Roming, P. W. A., Kennedy, T. E., Mason, K. O., et al. 2005, *SSRv*, **120**, 95
- Schlaflly, E. F., & Finkbeiner, D. P. 2011, *ApJ*, **737**, 103
- Scopatz, A. M., Romano, P. K., Wilson, P. P., & Huff, K. D. 2012, *Trans. ANS*, **107**, 985
- Shivvers, I., Mazzali, P., Silverman, J. M., et al. 2013, *MNRAS*, **436**, 3614
- Silverman, J. M., Foley, R. J., Filippenko, A. V., et al. 2012, *MNRAS*, **425**, 1789
- Smartt, S. J. 2015, *PASA*, **32**, E016
- Smartt, S. J., Eldridge, J. J., Crockett, R. M., & Maund, J. R. 2009, *MNRAS*, **395**, 1409
- Smith, K. W., Srivastav, S., McBrien, O., et al. 2020, TNSAN, **166**, 1
- Smith, K. W., Srivastav, S., Smartt, S. J., et al. 2021, TNSAN, **235**, 1
- Springob, C. M., Haynes, M. P., Giovanelli, R., & Kent, B. R. 2005, *ApJS*, **160**, 149
- Stahl, B. E., Zheng, W., de Jaeger, T., et al. 2019, *MNRAS*, **490**, 3882
- Stanway, E. R., & Eldridge, J. J. 2018, *MNRAS*, **479**, 75
- Stetson, P. B. 1987, *PASP*, **99**, 191
- Tonry, J. L., Stubbs, C. W., Lykke, K. R., et al. 2012, *ApJ*, **750**, 99
- Tonry, J. L., Denneau, L., Heinze, A. N., et al. 2018, *PASP*, **130**, 064505
- Valenti, S., Sand, D., Pastorello, A., et al. 2014, *MNRAS: Letters*, **438**, L101
- Valenti, S., Sand, D., Stritzinger, M., et al. 2015, *MNRAS*, **448**, 2608
- Valenti, S., Howell, D. A., Stritzinger, M. D., et al. 2016, *MNRAS*, **459**, 3939
- Van Dyk, S. D. 2017, *RSPTA*, **375**, 20160277
- Van Dyk, S. D., Davidge, T. J., Elias-Rosa, N., et al. 2011, *AJ*, **143**, 19
- Van Dyk, S. D., Zheng, W., Fox, O. D., et al. 2014, *AJ*, **147**, 37
- Van Dyk, S. D., Zheng, W., Maund, J. R., et al. 2019, *ApJ*, **875**, 136
- Vaucouleurs, G. d., Vaucouleurs, A. d., Buta, R., Ables, H. D., & Hewitt, A. V. 1981, *PASP*, **93**, 36
- Vogl, C., Kerzendorf, W. E., Sim, S. A., et al. 2020, *A&A*, **633**, A88
- Vogl, C., Sim, S. A., Noebauer, U. M., Kerzendorf, W. E., & Hillebrandt, W. 2019, *A&A*, **621**, A29